

2016-01-01

Digital Processes and Characterization for Fabricating 3D RF Devices

Harvey Hing Tsang

University of Texas at El Paso, hhtsang@miners.utep.edu

Follow this and additional works at: https://digitalcommons.utep.edu/open_etd



Part of the [Electrical and Electronics Commons](#)

Recommended Citation

Tsang, Harvey Hing, "Digital Processes and Characterization for Fabricating 3D RF Devices" (2016). *Open Access Theses & Dissertations*. 769.

https://digitalcommons.utep.edu/open_etd/769

This is brought to you for free and open access by DigitalCommons@UTEP. It has been accepted for inclusion in Open Access Theses & Dissertations by an authorized administrator of DigitalCommons@UTEP. For more information, please contact lweber@utep.edu.

DIGITAL PROCESSES AND CHARACTERIZATION FOR FABRICATING 3D
RF DEVICES

HARVEY HING-CHEONG TSANG, M.S.E.E.

Doctoral Program in Electrical and Computer Engineering

APPROVED:

Raymond Rumpf, Ph.D., Chair

Kenneth Church, Ph.D.

Namsoo David Kim, Ph.D.

David Zubia, Ph.D.

Charles Ambler, Ph.D.
Dean of the Graduate School

Copyright ©

by

Harvey H. Tsang

2016

Dedication

I would like to dedicate this dissertation to my family. For they shaped me into the person I am today with their love and support. I would like to thank all my friends for the great memories we shared that keep me functioning during the lonely nights. And special thanks to Dr Cesar Garcia, David Hsu, and Lizzie Liu who made the extra effort to keep me on track. And finally to my late dear friend Neil Patel, whose early departure has taught me to value each day and to never give up and never surrender.

DIGITAL PROCESSES AND CHARACTERIZATION FOR FABRICATING 3D RF
DEVICES

by

HARVEY HING-CHEONG TSANG, M.S.E.E.

DISSERTATION

Presented to the Faculty of the Graduate School of

The University of Texas at El Paso

in Partial Fulfillment

of the Requirements

for the Degree of

DOCTOR OF PHILOSOPHY

Department of Electrical and Computer Engineering

THE UNIVERSITY OF TEXAS AT EL PASO

December 2016

Acknowledgements

I am thankful for my advisor, Dr Church, who has continuously provided me with guidance and help needed to traverse through these past 7 years. He kept me focused and shielded me from the distractions and I am grateful for his hard-work, patience and faith in me. I am also thankful for my other advisor, Dr Rumpf, who has been encouraging and inspiring throughout these years with his intrepid support and help. His knowledge, experience and his selflessness has provided a nurturing environment to learn and continue pursuing my academics. I would like to thank my committee members for participating in my defenses and providing constructive criticism to my work.

I am also greatly thankful for my colleagues and mentors at the University of South Florida. I would like to personally thank Dr Tom Weller, Dr Nathan Crane, and Dr Craig Lusk for their help and leadership at my time in USF. I would like to acknowledge the work I did with Dr Ibrahim Nassar, Justin Nussbaum, Patrick Nesbitt, Thomas Ketterl and Eduardo Rojas. For without their help, this work would not exist.

Special thanks to all of my colleagues at nScrypt and Sciperio, your help, friendship and interactions has helped me grow into an engineer and a resilient person.

Abstract

In this work, co-planar waveguides (CPW) are fabricated and characterized with low temperature 3D printed materials for flexible electronic applications. Laser processing is introduced to reduce heating and cooling times for curing and subtractive manufacturing. CPWs are optimized by varying printing resolution, adjusting curing conditions and shaping conductor profile with a pico-laser. By using acrylonitrile butadiene styrene (ABS) as substrate material and Dupont CB028 as conductive material, a high S_{21} and low S_{11} CPW is fabricated. Optimized direct write methods are dispensed onto 3D complex structures to move away from 2.5D style printing and move into true 3D printed antenna devices.

Table of Contents

Acknowledgements	5
Abstract	6
Table of Contents	5
List of Tables	7
List of Figures	8
Chapter 1: Introduction	1
1.1 Motivation.....	1
1.2 Contributions.....	1
1.3 Dissertation Organization	3
Chapter 2: Background	4
2.1 3D Printing.....	4
2.2 Direct Print Additive Manufacturing of Conductors	10
2.3 Direct Digital Manufacturing of Electronics	14
Chapter 3: 3D Printed Dual-Channel Antennas.....	23
3.1 3D Printed Dual-Channel Circular Patch Antenna Array with Miniaturization.....	23
3.2 Quasi-Yagi Dipole Antenna (QYDA) Array	26
3.2.2 Conclusion	30
3.3 Log-Periodic Dipole Antenna (LPDA) Array.....	31
3.4 Conclusion	34
Chapter 4: Laser Ablation on Co-Planar Waveguide	36
4.1 Introduction.....	36
4.2 Laser settings	39
4.3 Fabrication Process	41
4.4 RF Conductivity Measurements	42
4.5 Conclusions.....	43
Chapter 5: 3D Printed Multi-Material Broadband Structural Current Sheet Antenna Array	45
5.1 Introduction.....	45
5.2 Initial Design.....	46

5.3 FFF Printability of the Unit Cell.....	48
5.5 Electrical Design and Fabrication.....	52
5.5 Conclusion	56
Chapter 6: Summary and Recommendations for Future Work	57
6.1 Summary	57
6.2 Recommendations for Future Work.....	57
References.....	59
Vita	62

List of Tables

Table 1. Comparison of FR4, ABS and SLA electrical properties with glass transition temperature	6
Table 2. Comparison of direct write technology capabilities. From[18]–[20]	11

List of Figures

Figure 1. Slicing software converting a solid object to layers of paths	4
Figure 2. Stereolithography process	6
Figure 3. FFF or micro-dispensing nozzle in a typical printing process	7
Figure 4. Extrusion DW system using the syringe system and controlled back pressure [21]	12
Figure 5. nScript, Inc. SmartPump valve assembly [23]	12
Figure 8. SEM of CB028 on ABS at x30 zoom conducted at USF	15
Figure 9. SEM of CB028 on ABS at x500 zoom conducted at USF	16
Figure 10. Model of the under extrusion (top) and over-extrusion (bottom) of ABS below the CB028 layer	17
Figure 12. Conductive traces printed on the bottom of the ABS sample (top), and printed on the top of the ABS sample with top lines running perpendicular (middle) and parallel (bottom)	19
Figure 13. Basic co-planar waveguide (CPW) fabricated with Direct Print Additive Manufacturing (DPAM).....	20
Figure 14. Simulated return loss (left) and insertion loss (right) of CPW with ideal materials and smooth surface modeled in AnsoftHFSS.....	20
Figure 15. Measured S-parameters of three CPW samples measured at the WAMI center at USF.....	21
Figure 16. Design (left) and fabricated (right) microstrip (MS) line.....	22
Figure 17. WAMI at USF Measured microstrip line design (left) and fabricated 3D microstrip line on ABS (right).....	22
Figure 18. Fabricated dual-channel circular patch antenna array	24
Figure 19. Side view of height varying profile*	25
Figure 20. Side View (Top) and Top view of the miniaturized (left) and planar CPA (right)	25
Figure 21. Fabricated Quasi-Yagi dipole antenna array (left) with top view of design (right)	27
Figure 22. Progression in PCAD of line fill order for even homogeneous fill factor.....	28
Figure 23. EFD tip options.....	29
Figure 24. 3D printed 45° attachment	29
Figure 25. Design of the quasi-Yagi antenna with dimensions	30
Figure 26. Trimetric view (left) and top view (right) of 3D printed LPDA array	33
Figure 27. Classic beam-matter interaction	37
Figure 28. Ultra-short pulse laser-matter interaction.....	37
Figure 29. Laser ablated profile with regions of temperatures exceeding sintering temperatures of 1234.15K (961°C).....	38
Figure 30. a) SEM performed at USF of edge of micro-dispensed paste without laser processing, b) SEM performed at USF of laser ablated slot with visible region of sintered silver particles, c) SEM performed at USF of laser machined slot, and d) 3D profile of a laser machined slot[43]	42
Figure 31. (a) Micrograph of CB028 showing the laser-treated area, (b) electrical conductivity of CB028 film using the DR-based NFMM and (c) measured surface topography[43].....	43
Figure 32. 2x4 element 2-18 GHz current sheet antenna with bottom view (left) and top view (right) of an individual unit cell	45
Figure 33. Comparison of fabrication tolerances of 4 GHz design (white) with 2 GHz (black).....	47
Figure 34. Balun-fed 4 GHz antenna designs a) conventional microstrip b) 3D printed without ground plane c) 3D printed with ground plane d) 3D printed with FSS ring and ground plane.....	48
Figure 35. 3D printed coax structures (left) with optical microscopic view of inner roughness (right)	49

Figure 36. 3D printed unit cell with sagging and curled edges on top substrate.	49
Figure 37. Final unit cells with FSS ring	50
Figure 38. 1x3 array of unit cells printed for mechanical testing	51
Figure 39. Reinforced 1x3 array for longitudinal testing	51
Figure 40. Unit cell prints of bowtie and coaxial transition (left) topside on the left with bottom side on the right with conductivity check performed with a multimeter (right)	52
Figure 41. Top view (left) and bottom view (right) of the coaxial transition test coupons with tuned printing parameters. SMA connectors were attached for RF measurements.	53
Figure 42. Unit cell separated for modular printing bottom with coaxes (left) and FSS with top substrate (right)	54
Figure 43. DW extrusion process of FSS layer on 2x4 array	54
Figure 44. 3D printed unit cell antenna test samples	55

Chapter 1: Introduction

3D printing has multiple uses in variety of areas including tissue engineering, mechanical structures, textiles, food and even electronics. 3D printed electronic devices are currently challenging to fabricate due to material performance and the lack of process compatibility. Most of the desired materials for electronics are polymer based and have limited post process temperature capability. Additionally, the majorities of printable conductive materials requires higher temperature processing or have inferior performance. Printed electronic devices in the RF regime are especially challenging due to the need for good RF properties of both the dielectric and the conductors. Surface features in RF devices can also negatively affect the performance therefore smooth surfaces and straight conductor edges must be considered. These are issues for 3D printing given the fundamental process of layer by layer printing. The advantages of overcoming these barriers are several, including more functions per volume, reduced weight, reduced time from design to product and ultimately reduced cost.

1.1 Motivation

Additive manufacturing (AM) is a rapidly expanding component of the advanced manufacturing sector that is transforming the product development cycle across a wide spectrum of industries. AM continues to present strong patterns of expansion, with growth rates in the double digits, thus carrying substantial economic and job growth impact [1]. Among a variety of available AM processes, micro-dispensing and fused filament fabrication (FFF) have perhaps the widest application domains owing to their low process temperatures, dimensional versatility and wide availability of compatible materials. The combination of AM techniques together with other digitally-controlled processes constitutes the more general classification of Direct Digital Manufacturing (DDM).

1.2 Contributions

The main contributions from the work fall within the following categories:

- i) Development of harmonic transceivers with novel printing techniques with existing direct write (DW) technology.

To the best of the author's knowledge, the developed harmonic transceivers have the best overall performance among previously conventionally manufactured published designs, in terms of conversion gain, communication range, and occupied electrical volume. These are achieved through the utilization of novel printing techniques which enable the deposition of conductive material onto complex structures with obstructing features.

- ii) Adding value to the study of new DDM techniques for the purpose of 3D printed electronics.

The simulation and experimental results of 3D printed co-planar waveguide transmission lines have yielded an understanding of the limitations of 3D printed materials. A new approach to the fabrication of electrically improved CPW transmission lines which is compatible with the additive manufacturing process.

- iii) Addressing the environmental effects on the electrical performance of 3D printed materials

Tensile, compressive and temperature cycling tests of 3D printed materials are conducted onto electronic devices with inspection to the changes to their electrical characteristics.

- iv) Showing the advantages of the use of multi-material digital additive manufacturing for the fabrication of complex and efficient RF devices

The digital additive manufacturing technology has been used in the design of 3D antennas, transmission lines, and arrays antennas, while enabling the realization of low-cost, light-weight, robust, efficient, miniaturized RF devices with comparable or improved manufacturing reliability, repeatability and flexibility.

1.3 Dissertation Organization

This dissertation is divided into six chapters. Chapter one introduces the work in this dissertation and Chapter six summarizes the content of this research.

Chapter two provides the background information of current 3D printing processes and materials. A small range of materials are discussed and substrate and conductor materials are selected for the remainder of this dissertation. A co-planar waveguide (CPW) and a microstrip (MS) line designs were fabricated and tested for 3D material compatibility.

Chapter three covers research on dual-channel transceiver designs with conventionally FFF printed antennas with direct write extruded conductive paste. These novel transceivers utilize FFF printing to create their complex shapes. Novel direct write extrusion methods are also utilized to conformally pattern conductive pastes to these complex structures. The transceivers contain separate harmonic transceivers for sensing and to provide a reference signal (no sensor) for remote channel calibration and identification. Comparisons between the transceivers presented in this dissertation and with other designs from the literature are given.

Chapter four presents the CPW with the application of pico-second laser ablation process. The physical effects to the conductive material are imaged and the residual heat damage is modeled with the classical beam-matter interaction model to predict the temperature the conductive material reaches during the ablation process. The CPWs are tested and compared to the original CPW.

Chapter five covers an extensive study on the mechanical and electrical performance on a current sheet antenna array design through environmental changes. The array is printed with high resolution FFF printing and with multi-material printing. The unit cell of a current sheet antenna consists of a microstrip to coax transition feed network, bowtie antenna and frequency selective surface.

Chapter 2: Background

2.1 3D Printing

3D printing involves the process of depositing materials, usually plastics or metals, to form a 3D part. This process is additive but may include subtractive post-processes to tighten up parameters, such as surface roughness [2]. Before a part can be fabricated, a digital model of the part must be created. This can be done by hand through computer-aided design (CAD) software, such as Dassault Systèmes SOLIDWORKS, or through simulation software, such as ANSYS HFSS. Alternatively, a part can be created by scanning a real object and tweaked with a software tool, such as the Geomagic Print [3]. Despite how the part is digitally created, it must run through a ‘slicing software’, such as Slic3r [4], which divides the 3D object into multiple cross-sectional slices, of adjustable thickness, as shown in . These slices are converted with parameters for 3D printing that can be adjusted within the slicing software [3].

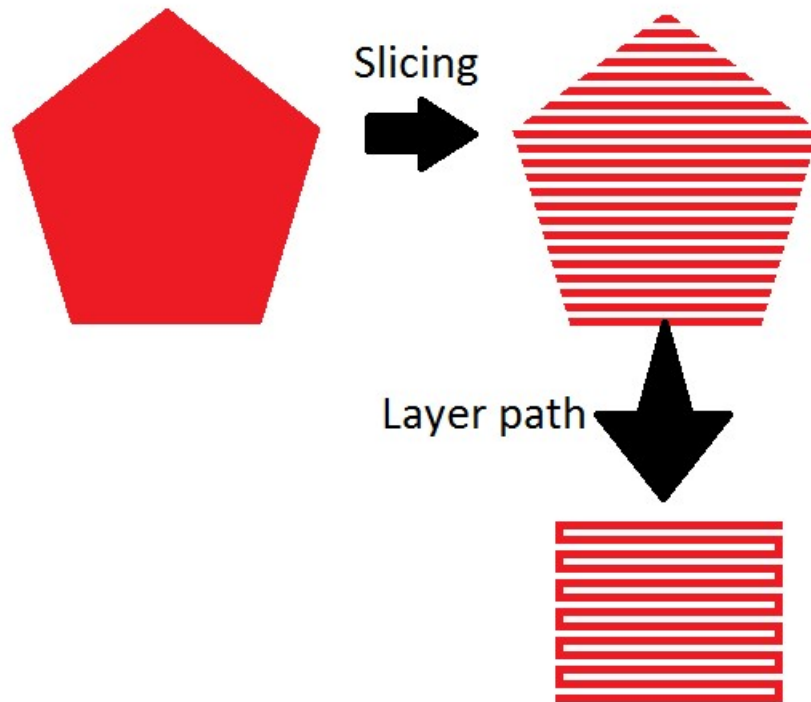


FIGURE 1. SLICING SOFTWARE CONVERTING A SOLID OBJECT TO LAYERS OF PATHS

The parameters of these files include print speed, extrusion width, and layer thickness. These new files generated by slicing are sent to the 3D printer and the slices are printed on top of one another. Different 3D printers use different forms of printing material and processes. The fused deposition modeling (FDM), or increasingly being referred to as fused filament fabrication (FFF) due to the Stratasys copyright to the acronym FDM, will be the focus of this work. This is due to its inherent advantages of cheap material costs, production speed, and design flexibility [5]. While the library of 3D printed materials expand everyday with better mechanical and electrical properties, FFF materials are characteristically less brittle [5] and have a lower loss tangent [6]. The greatest advantage of FFF parts is the little to no post-processing required to finalize the part. This characteristic allows FFF parts to be better suited for DDM. This term refers to 3D printers which can be used to fabricate ready-to-use parts. Many industries have started applying DDM to their products, such as the car, aerospace and toy industries [7]–[9].

In order to create electronic parts, we will need the AM of conductive traces and components. DW is the AM of conductive materials which enable the embedding of electronics in 3D printed parts. DW is the selective deposition and patterning of material, either by extrusion, inkjet or laser [10]. Direct Print (DP) is a similar term but used to refer to the printing with multiple nozzles, such as AM with DW, to achieve a 3D printed functioning device. In this work, the extrusion DW method will be the main focus. The greatest advantage of the extrusion DW method is its ability to print a wider range of materials at a greater thickness, comparatively.

2.1.1 PRINTING METHOD

2.1.1.1 FFF vs SLA

Stereolithography (SL) is a 3D printing process which utilizes a vat of viscous UV curable liquid resin with a submerged platform where a focused UV beam is directed to cure and thus create a solid part. As each layer is cured, the platform will further submerge and a wiper distributes material over the surface, before next layer curing, until the part is complete, as shown in Figure 2. Excess uncured material must be washed off with water. This procedure does

not easily incorporate other forms of 3D printing into its build cycle and while the uncured liquid can be used later, there must always be a minimum volume of material in the vat to keep the printing in progress. Eventually, this vat needs to be emptied and replenished with fresh liquid resin which is costly and wasteful.

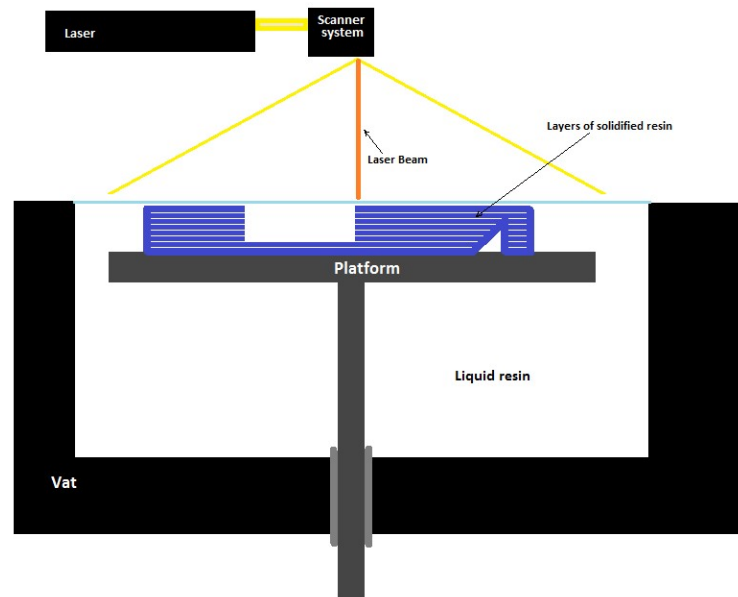


FIGURE 2. STEREOLITHOGRAPHY PROCESS

Commercial SL equipment can achieve 0.1016mm layer thickness and 0.254mm feature sizes[11]. An SL part is characteristically light, smooth and brittle. The electrical properties of standard SLA material are lossy with low dielectric constants[12], as shown in Table 1.

TABLE 1. COMPARISON OF FR4, ABS AND SLA ELECTRICAL PROPERTIES WITH GLASS TRANSITION TEMPERATURE

Material	Dielectric Constant	Tangent Loss	Max Temp °F
Conventional FR4	4.2 – 4.9	0.008 - 0.018	130 – 155
FFF (ABS)	2.0 – 3.5	0.005 – 0.019	171 – 228
SLA (NanoTool)	3.45	0.0114	135 – 144

From Table 1, it can be observed that ABS has the lowest dielectric constant, but has the potential for the lowest tangent loss and highest operational temperature. While some devices can use a high dielectric constant to create more isolation between signal lines, this dielectric constant would be beneficial in fast digital circuits where signal linearity and noise is less critical. With such comparable electrical properties, the FFF process would have the greatest advantage since FFF parts do not require a post-processing step to allow the printing of a conductive layer.

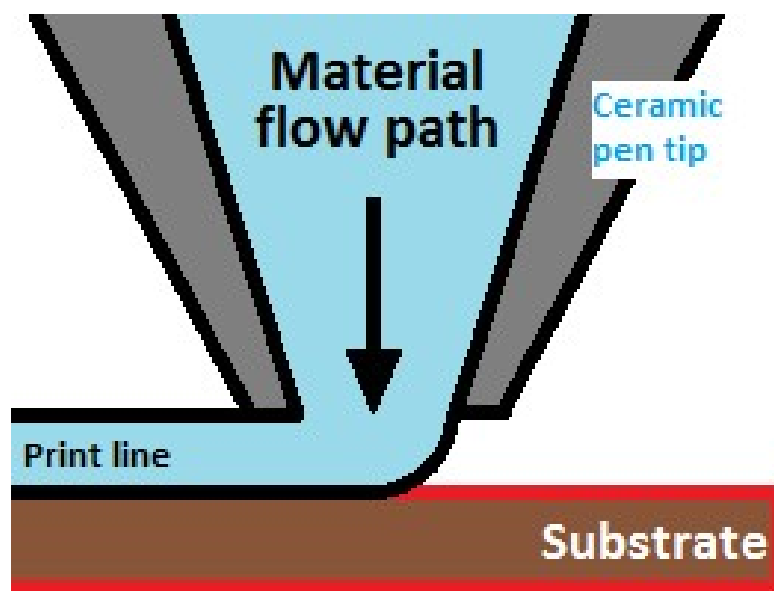


FIGURE 3. FFF OR MICRO-DISPENSING NOZZLE IN A TYPICAL PRINTING PROCESS

FFF involves extruding molten plastic, through a heated tip, which rapidly cools and solidifies providing the platform for the next layer. Material flow is controlled by a gear which pushes or pulls the plastic thread. After the part is finished, the bed needs to be cooled before the part can be taken off without deforming[13]. Initially, the molten plastic is dispensed onto a flat platform, known as the print bed. The first layer of the part is sometimes preceded by extra perimeters, either attached or detached from the part, known as the brim or skirt, respectively. The brim is used to provide a larger area of contact between the part and print bed for better adhesion. The extra brim material can be easily removed by hand or with a razor blade after the

print is finished. When there is no brim, a single layer of skirt can be used to normalize the printed line. This is more critical after long intervals between print jobs and when using small nozzle diameters, due to the slow expansion of molten plastic within the reservoir of the nozzle. Subsequent layers are built on top, layer upon layer, until the final part is complete. Depending on the features of the part, sometimes the nozzle will need to print over gaps. When printing over gaps, the extruded plastic cools and solidifies in mid-air. At this point, if the plastic line is under tension, a bridge can be built to connect two sides. Controlling the surrounding temperature, print speed and extrusion multiplier can produce bridging features with minimal sagging. Even after tuning these parameters, a solid platform can only be achieved with multiple layers and multiple adjacent lines. Longer bridging features can be achieved by increasing the width and thickness of the platform, as long as the sagging does not reach the floor and release the tension of the extruded line. When bridging features cannot be achieved through this process, a fine lattice of support structures can be built up to provide multiple shorter gap distances. These support features are usually easily removed by hand or by tweezers after the part is finished. FFF printers, with multiple material printing capabilities, can print soluble support materials. This method provides the best support but at the cost of a messy post-process to remove the soluble material, usually involving immersing and agitating the part in water till the support material is removed.

Conventional FFF parts come with limitations due to the FFF process. The layering process in FFF, produces noticeable stepping features and becomes more apparent on sloping features. These issues are usually magnified with low resolution and low accuracy printing. A smooth finish is conventionally achieved with sanding or chemically treated, but these post-processes are not easily applied for embedded features. Some printers remedy this by printing with a high resolution, but the improvement in surface finish is usually hard to be justified and result in significant increase in build times. For example, a 0.05 mm high resolution print takes twice as long as a 0.1 mm medium resolution print. Some parts may forego its surface finish for

faster fabrication, and with some functional parts, the surface finish is irrelevant, e.g. door stop, shelf bracket, etc.

Depending on material, FFF parts are usually susceptible to warping, shrinking or curling during the print. To remedy this, most FFF printers are installed with heated print beds to raise ambient temperature and reduce temperature gradients that vary cooling rates. The build area can also be enclosed to prevent drafts. In some chapters of this study, the added use of ceramic space heaters to provide a flow of hot air to quickly bring thermoplastic temperatures below their glass transition point (approx. 221 °F for ABS), whilst keeping the ambient temperature at around the same point. An alternative method to reducing warping is by adding fans directed at the print head to rapidly cool plastic that was just printed. By slowing the print head speed, the exposure time to the fans increase and further reduce warping issues. Most printers have resolved or significantly reduced this issue for most features and parts. Large thin features are still susceptible to warping and curling though.

FFF parts are also known have weaker adhesion between adjacent lines and especially in the Z-direction, top and bottom layers. This delamination issue is alleviated by alternating print directions by 90 degrees every layer, improving the tensile strength along the X-Y plane, but the tensile strength in Z is significantly less. This is most effectively resolved by complicating the design of the part with separately printed interlocking pieces. But adjusting the extrusion multiplier can adjust the volume of molten plastic dispensed out of the nozzle at a time. Decreasing the extrusion multiplier reduces the volume of material, and when decreased from optimal printing settings, would result in the under-extrusion of material. This is usually undesired and would be removed during the tuning process. Increasing the extrusion multiplier increases the volume of molten plastic dispensed out of the nozzle. When increased from optimal printing settings, would result in the over-extrusion of material. This results in a more solid part, but at the exchange of rougher surface finish.

FFF parts come with An FFF part is characteristically more resistant to impact, more porous, and with a rougher surface compared to its SL counterpart. FFF parts do not require

further post-processes but mechanical or chemical surface smoothing methods are common and parameter tuning can alleviate or even eliminate solid infill issues. The electrical properties of standard FFF material are comparable to FR4 with similar losses and dielectric constants[6].

2.2 Direct Print Additive Manufacturing of Conductors

3D printable conductive materials range from aerosolized low viscous inks to thick-film pastes and further to conductive FFF filament [14]–[16]. Aerosolized low viscous inks usually contain nano-sized particles [17] which need to be atomized, in order to be carried by gas which is then directed towards a substrate [18]. These inks usually require high curing temperatures exceeding the glass transition point of ABS, 105 °C, but can produce low resistivity traces, 5 mΩ/sq/mil @ 250 °C [19].

Conductive filaments can be FFF printed and are compatible with other FFF materials. Their high resistivity makes them unviable as conductive material for electronics, 76 mΩ/sq/mil [20].

For thick-film pastes, in general, these materials contain solid conductive particles ranging from the nanometer to micrometer sizes. These particles are suspended into a mixture of solvents and binders which keep these solid particles in relatively uniform distribution and can adhere the solid particles to each other and to the substrate. DupontCB028 is a silver flake conductive paste, which relies on micron sized silver particles to contact and form the conductive path. This paste is normally cured at 160°C for 1 hour to drive off the solvents in the out-gassing procedure which incurs a total mass loss of 0.18% [15]. It also has a low resistivity, of 7-10 mΩ/sq/mil, when compared with the other types of inks and pastes [21]. The mass loss allows the remaining material to contract and bring the silver flakes into physical contact, as shown in [22]. CB028 has a viscosity of 15000-30000 cP which makes it only suitable for the DW extrusion method as described below. There are other conductive inks that have similar properties but with even lower resistivity 4 mΩ/sq/mil [23], but they require an extra PulseForge step, which was not available when these studies were conducted.

DW is a non-contact deposition process that enables selective patterning of material onto flat or conformal surfaces [24]. DW technologies range from inkjet, aerosol jet, and extrusion methods, which produce features ranging from the nano-meter to the milli-meter range. DW methods are capable of dispensing non-conductive materials, such as ceramic, epoxy and biomaterial. But this study will focus only on the printing of conductive material.

TABLE 2. COMPARISON OF DIRECT WRITE TECHNOLOGY CAPABILITIES. FROM[18], [25], [26]

Technology	Minimum Resolution	Viscosity Range	Max Write Speed	Layer Thickness
Inkjet	$\geq 20 \mu\text{m}$	$\leq 0.1 \text{ Pa}\cdot\text{s}$	$0.3 \text{ mm}^3/\text{s}$	$\sim 14 \mu\text{m}$
Aerosol	$\geq 10 \mu\text{m}$	$\leq 0.1 \text{ Pa}\cdot\text{s}$ & can be atomized	$0.25 \text{ mm}^3/\text{s}$	10 nm
Extrusion	$\geq 25 \mu\text{m}$	$\leq 5000 \text{ Pa}\cdot\text{s}$	300 mm/s	0 – 200 μm

From Table 2, we can compare the physical constraints of each of the DW technologies. While aerosol can print the highest resolution, it also prints the slowest, just like the FFF process. Inkjet and aerosol processes involve dispensing droplets of material which limit the range of material choices to only those which have low viscosity or can be atomized. While these numbers are a general rule, most of these values would be dependent on the material. Extrusion DW will be the main focus of these studies since printing resolutions will be on the order of 150 μm , which is the 1/100 wavelength, for 20 GHz maximum electrical performance.

2.2.1 PRINTING PROCESS

Extrusion DW is similar to FFF in that both use pressure to push material through a small nozzle, as shown in Figure 3. This is the most versatile of the DW technologies due to its printable range of material viscosities. This allows different recipes of material to be mixed to produce a wide range of characteristics. The basic extrusion DW method is the attachment of a

nozzle to a syringe and through a plunger or pressure system, pushes material out, as shown in Figure 4.

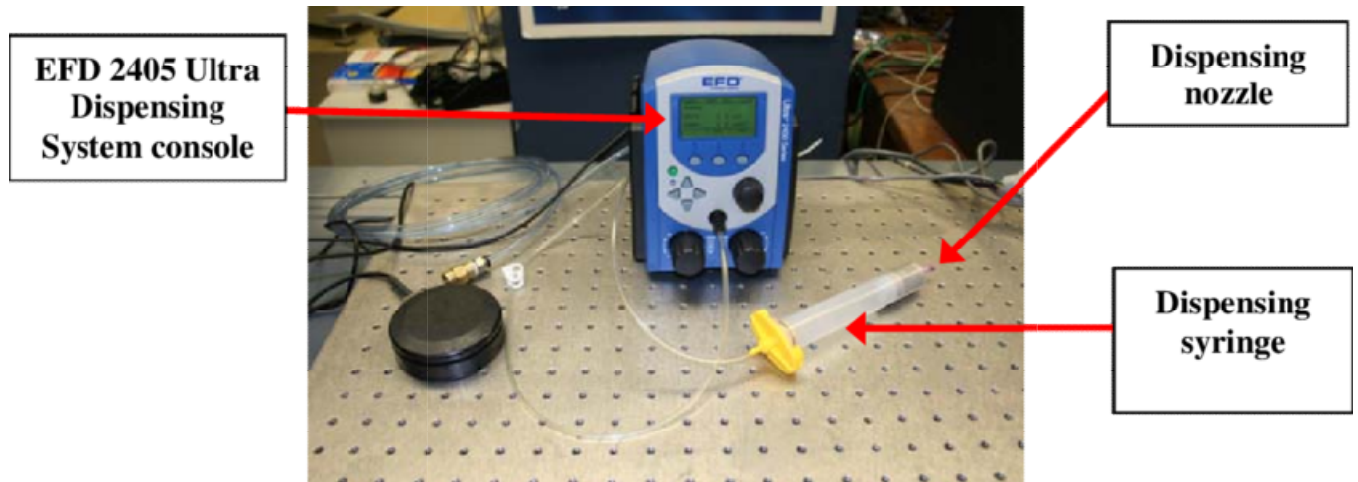


FIGURE 4. EXTRUSION DW SYSTEM USING THE SYRINGE SYSTEM AND CONTROLLED BACK PRESSURE [27]

Other systems use an additional valve system to control the output volume of material, as shown in Figure 5. The nScript SmartPump can micro-dispense at print speeds of 300 mm/s, although 20 mm/s is more commonly used, with volume control as low as 100 picoliters[28].

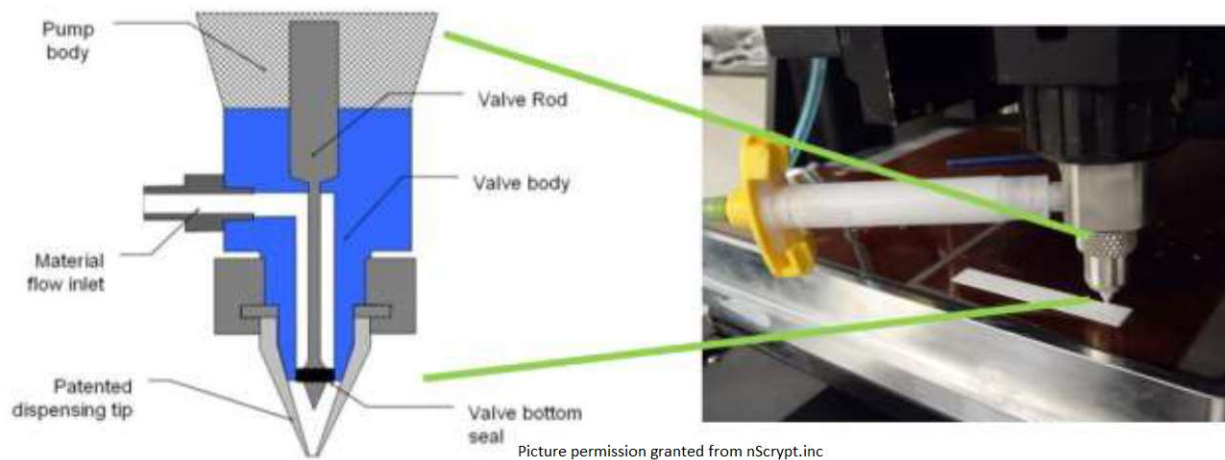


FIGURE 5. NSCRIPT, INC. SMARTPUMP VALVE ASSEMBLY [29]

The nScript printer system also starts with a digital model of the pattern. This can be tweaked and imported into their pathing software, which converts large print areas into

serpentine lines of fixed width. This width would be decided through the tuning process when printing with new materials. This print file is then sent to the printer where the user can adjust the valve settings, print speed and pressure before printing. The most crucial parameter is the dispense gap between the nozzle and the substrate, there is an optimal offset for the dispense tip, within the diameter of the pen tip [27], [30]. This dispense gap can be limited by the printing quality of the FFF process.

2.2.2 PATHING ISSUES

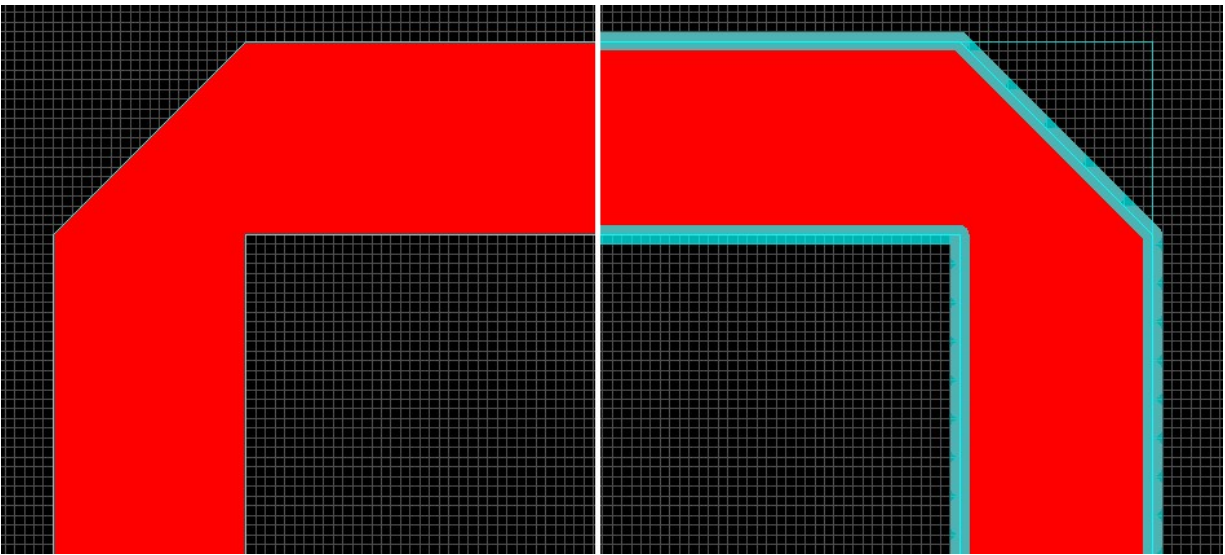


FIGURE 6. ACTUAL DESIGN (LEFT) WITH HIGHLIGHTED PERIMETER WITH PEN WIDTH CONSIDERATION (RIGHT) WITH STANDARD PATHING PROCEDURES

From Figure 6, we can observe that due to the width of the printed line, the perimeter is enlarged by exactly half of the diameter of designed pen width. This occurs due to the inherent vector pathing in the Path2D.exe program. Without adjusting for this phenomena, fabricated dimensions will always print excess material which will fatten solid dimensions and decrease critical void sizes, e.g. via diameters. The decrease in void features, such as via diameters, are resolved through an arc compensation [31]. While this method is usually used for FFF printing, the theory can be applied to DW paths to eliminate the shrinking of void features.

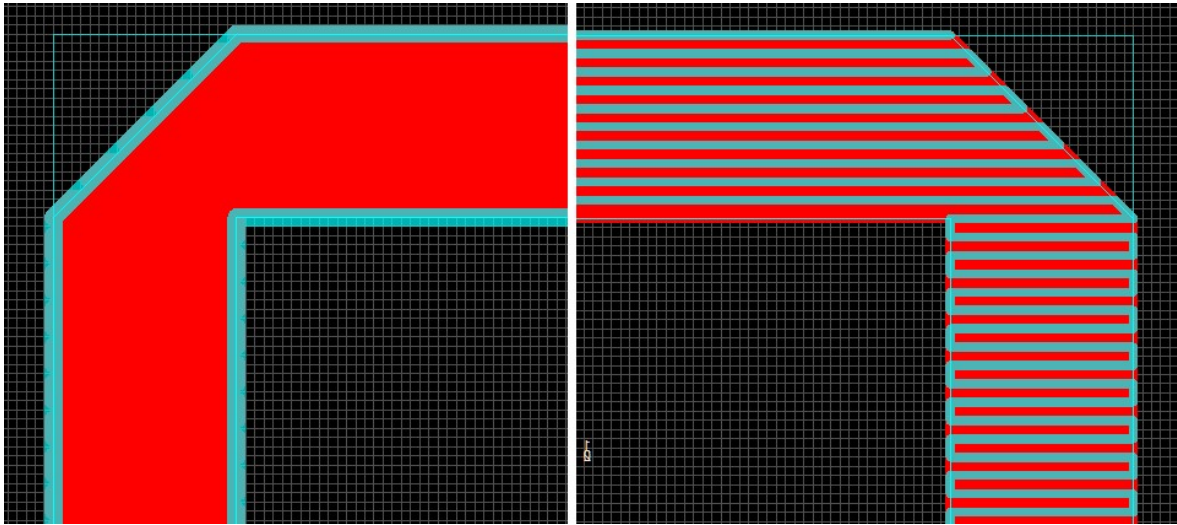


Figure 7. Design with highlighted perimeter path in blue (left) compared with standard procedures for infill path in blue (right)

From Figure 7 the infill line widths have been visually reduced from 0.2 mm to 0.1 mm to illustrate the path, we can observe multiple infill paths overlapping pre-existing ones on the perimeter. This overlay will cause a buildup of excess material in these regions, affecting the thickness and possibly the width of the print line. This infill path is redesigned with minimal overlapping near the perimeters and any inconsistencies resolved within the center of trace paths.

In ideal conditions, the acceleration of the print head is infinite and speed is constant during the whole printing process. In actual printing conditions, the print head undergoes deceleration as it approaches turns and acceleration as it leaves them. This can lead to buildup and thinning of material in these regions. The nScript stages attempt to remedy this by preparing counter motors to “knock” the tool plate into its intended direction. This large opposite force increases the deceleration and acceleration greatly. But to minimize this issue in design, we can reduce right-angled turns and remove any successive right-angled turns, i.e. “U-turns”. The solutions to these issues are demonstrated in Chapter 3.

2.3 Direct Digital Manufacturing of Electronics

From Figure 8 and Figure 9, the SEM scans were captured at the University of South Florida (USF) by Justin Nussbaum. The ABS is the darker material on the bottom and the conductive paste, DupontCB028, is the lighter material on the top. We can observe that the

dispensed CB028 settles into the voids of the ABS surface which is where the energy concentrates at higher frequencies. This shows that the DW method is dependent on the porosity of ABS and degradation of high frequency electrical performance can be expected, but this should not be an issue in this work according to the studies in [32], [33]. The silver flakes in the lighter sections are distributed quite consistently and antennas perform very well using this material even with the uneven geometry on the micron scale, shown in Chapter 3: 3D Printed Dual-Channel Antennas.

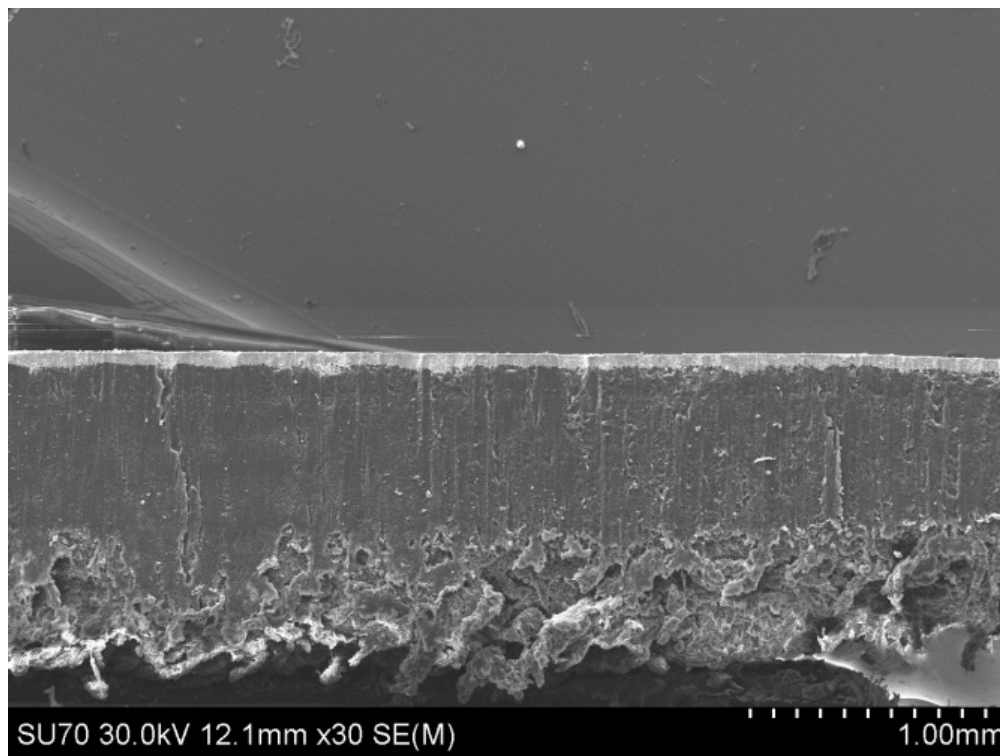


FIGURE 8. SEM OF CB028 ON ABS AT X30 ZOOM CONDUCTED AT USF

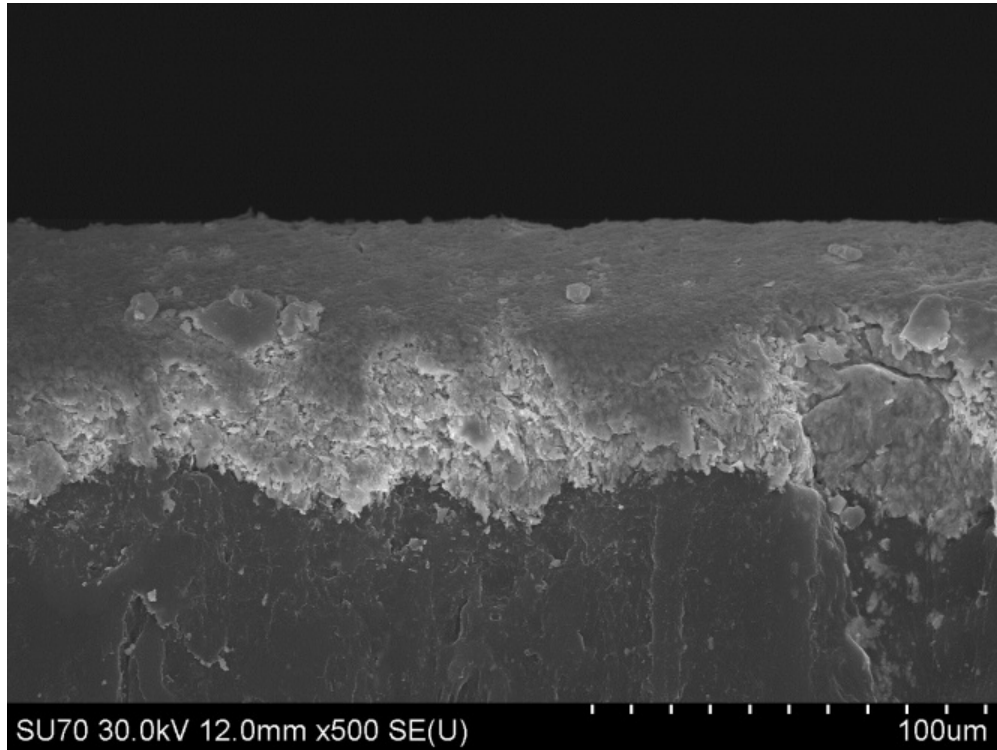


FIGURE 9. SEM OF CB028 ON ABS AT X500 ZOOM CONDUCTED AT USF

From Figure 10, we can observe the issues with under- and over-extrusion at the ABS/CB028 interface. When ABS is under-extruded, the gaps between each line provide a void for the CB028 to move into, due to surface tension. This can lead to bleeding of conductive material between layers, possibly causing a short. During over-extrusion, the over-extrusion marks can cut the traces and create an open circuit. At best, these FFF issues will increase the electrical path of the traces, thus incurring more resistive losses. Tuning the extrusion multiplier, extrusion width and print speed, for a specified nozzle diameter and temperature, can produce prints with neither under- or over-extrusion.

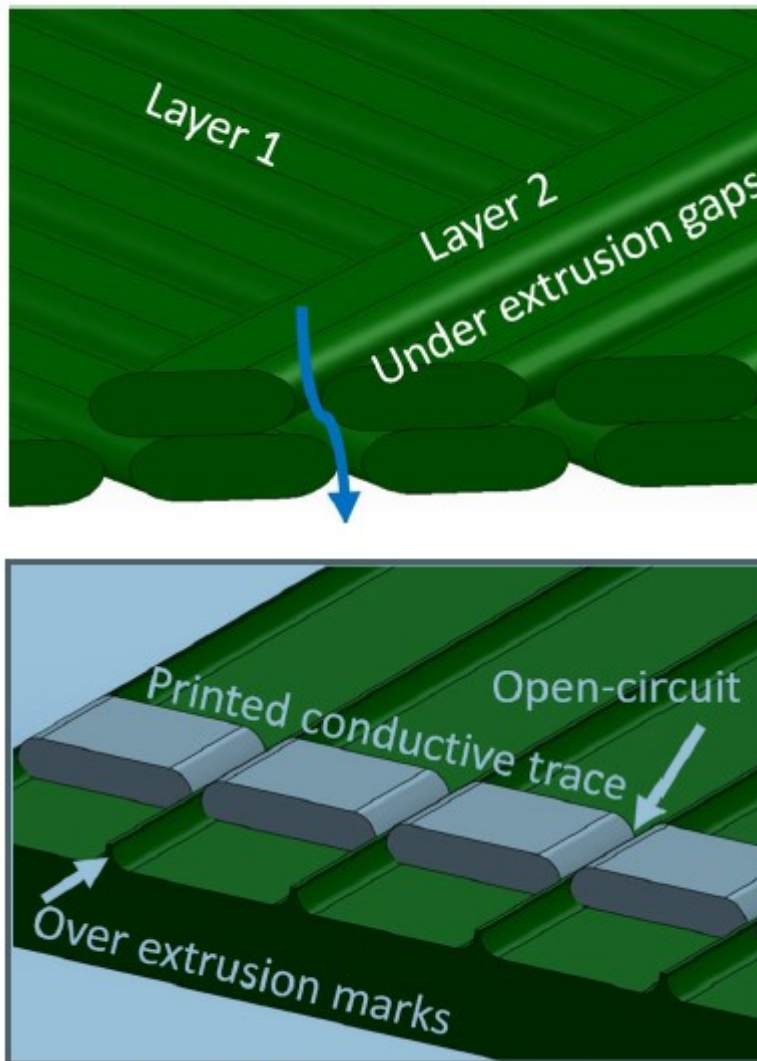


FIGURE 10. MODEL OF THE UNDER EXTRUSION (TOP) AND OVER-EXTRUSION (BOTTOM) OF ABS BELOW THE CB028 LAYER

The surface roughness of FFF parts can also be determined by the top layer printing orientation. Due to the nature of FFF printing, the surface ridges can be parallel, perpendicular, or a combination of both to electrical traces. From Figure 11, we can see how these lines run compared to a conductive trace.

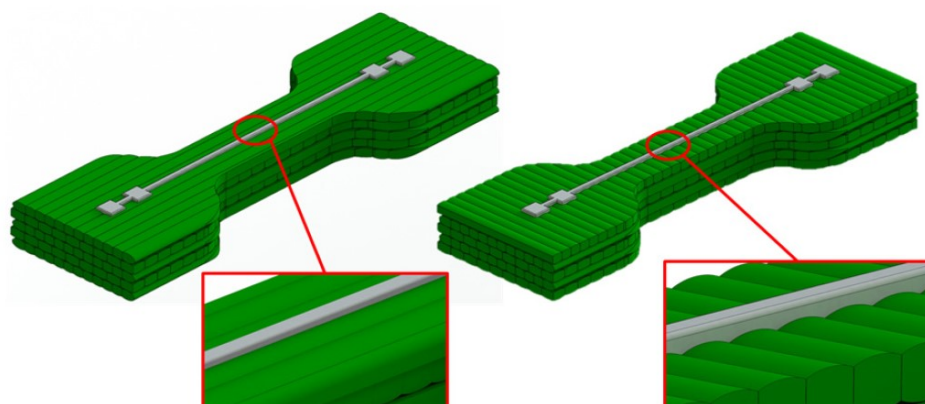


FIGURE 11. DIFFERENT PLASTIC PRINTING ORIENTATIONS WITH CONDUCTIVE TRACES (LEFT) PARALLEL AND (RIGHT) PERPENDICULAR TO DEPOSITION LINES[34]

Multiple test coupons were printed at 100 % infill and 2 shells with a 75/125 μm ID/OD nTip and printed with 0.1 mm extrusion width and 0.05 mm layer thickness, as shown in Figure 12. After the parts were cooled to room temperature, DuPont CB028 was dispensed out of a 125/175 μm ID/OD nTip and tuned for 0.2 mm extrusion width and 0.1 mm layer thickness before curing. These test coupons were cured at 60 °C for an hour. These test coupons were created to measure the effect strain would have on the electrical performance of the CB028 based on surface roughness of the part and the print orientation. The coupon with the smoothest surface finish has CB028 dispensed onto the surface of the test coupon that was in contact with the heated bed during printing. Five of these test coupons were printed this way. Five of the coupons were printed with the top surface deposition lines running along the long axis and five printed with the top surface deposition lines running perpendicular to the long axis. These test coupons are shown in Figure 12. These coupons were pulled while measuring for resistivity.

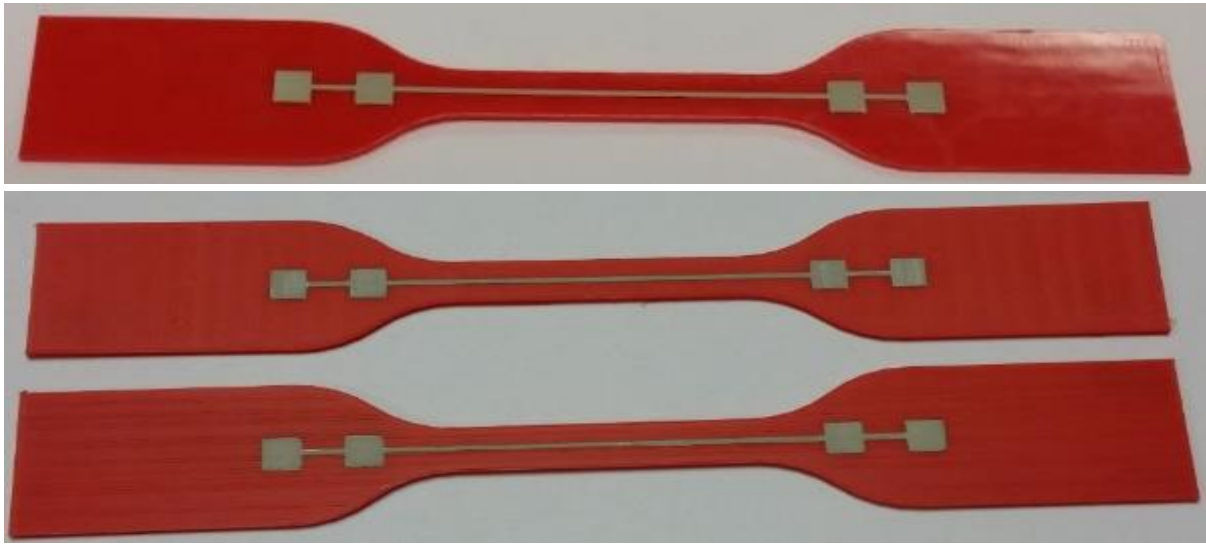


FIGURE 12. CONDUCTIVE TRACES PRINTED ON THE BOTTOM OF THE ABS SAMPLE (TOP), AND PRINTED ON THE TOP OF THE ABS SAMPLE WITH TOP LINES RUNNING PERPENDICULAR (MIDDLE) AND PARALLEL (BOTTOM)

The length of the conductive trace was chosen to be 49 mm which was calculated to give a resistance of approximately 0.8Ω . The antenna's bottom plane is 1 mm thick and was also used as the thickness of the tensile test coupon.

Traces parallel to the printed filaments showed the lowest resistivity of 0.7Ω , next was the smoothest surface at 0.8Ω and finally the perpendicular surface resulted in the highest resistivity, 1.7Ω . Traces perpendicular to the extrusion direction showed much higher resistance, higher variation and more sensitivity to mechanical strain. This occurs because the ink flows into the trenches between extruded lines creating thin, high resistance regions due to the poor coverage over the relatively rough surface of the extruded parts. These orientation dependent properties and structural/electronic coupling need to be characterized and be considered in designing reliable systems. With this knowledge, the polymer extrusion paths could be optimized to improve conductivity by aligning them to the paths of the electrical conductors.

Three CPWs of characteristic impedance of 50Ω were fabricated with Dupont CB028 onto ABS plastic. The ABS substrate was printed with conventional printing parameters, 0.3 mm

nozzle diameter and 0.1 mm layer thickness. The conductive layer was printed on top with signal width (W) of 1 mm and gap (G) of 0.1 mm, as shown in Figure 13. SMA connectors were attached and the parts were measured by the Center of Wireless and Microwave Information Systems (WAMI) at USF.

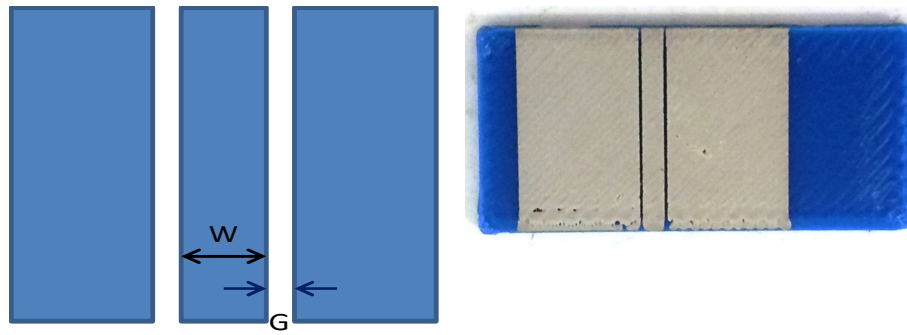


FIGURE 13. BASIC CO-PLANAR WAVEGUIDE (CPW) FABRICATED WITH DIRECT PRINT ADDITIVE MANUFACTURING (DPAM)

The CPW was simulated in HFSS with values of CB028 conductivity from [22] and using copper on FR4. The CPW is fed through modeled SMA connectors. The S-parameters were obtained with a frequency sweep between 12 – 18 GHz. These results can be observed in Figure 14.

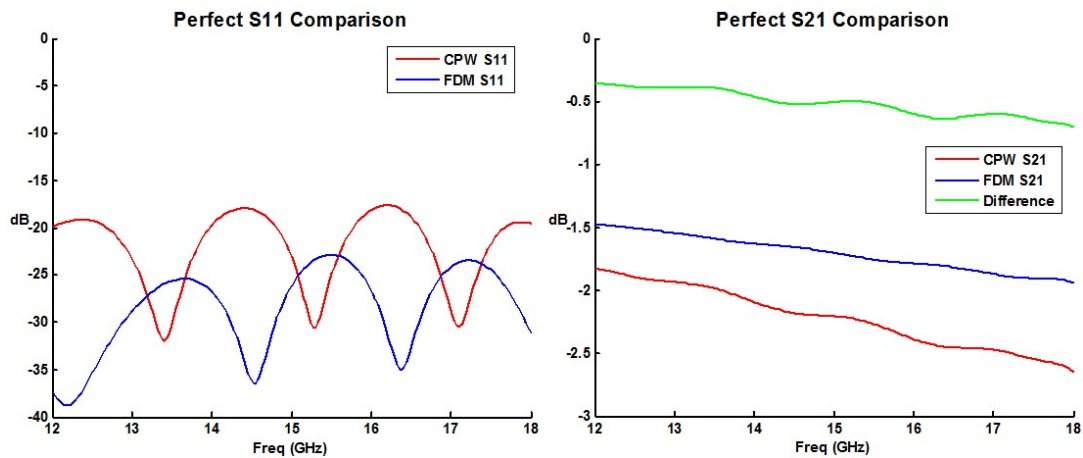


FIGURE 14. SIMULATED RETURN LOSS (LEFT) AND INSERTION LOSS (RIGHT) OF CPW WITH IDEAL MATERIALS AND SMOOTH SURFACE MODELED IN ANSOFT HFSS

From Figure 14, we can observe a frequency shift and minor performance loss when using the 3D printed material. Between 12 – 18 GHz, the insertion loss is around -25 dB and the return loss drops from -1.8 dB to -2.6dB. These are caused by the decreased dielectric constant of the ABS and the decreased conductivity of the CB028, respectively.

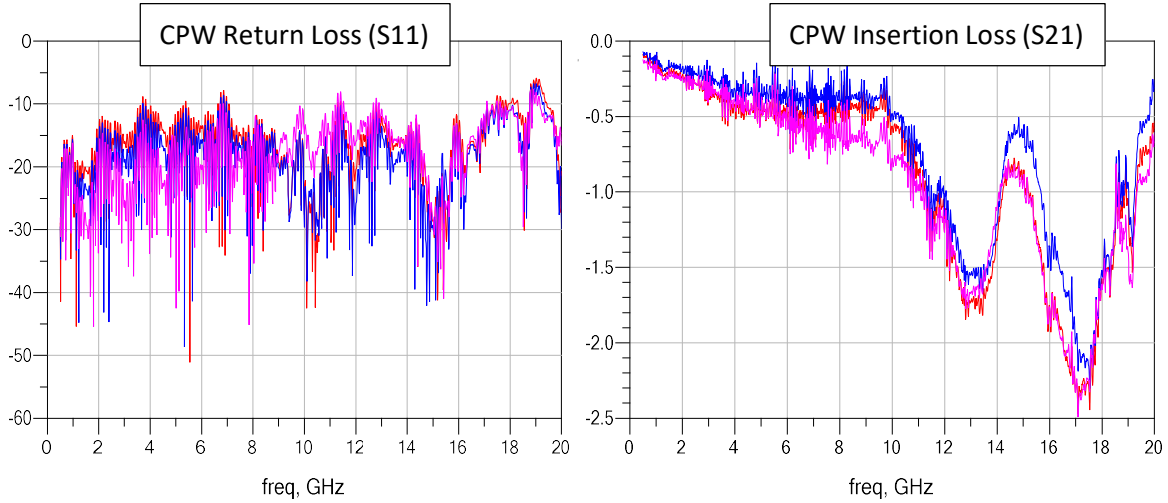


FIGURE 15. MEASURED S-PARAMETERS OF THREE CPW SAMPLES MEASURED AT THE WAMI CENTER AT USF

Figure 15 was measured by WAMI, the three samples show only minor deviation from each other. We can observe a return loss of -15 to -25 dB at 12 GHz and -10 to -11 dB at 18 GHz, but the samples maintain an approximate -30 dB between those ranges. Their insertion loss ranges from -1.1 to -1.2 dB at 12 GHz and approximately -1.5 dB at 18 GHz. Apart from the substantial ripples above 10 GHz, results match closely with simulated data when accounting for fabrication and testing errors. A more linear increase in loss is expected as frequency increases, similar to the simulated data provided in Figure 14.

Another common transmission line is the microstrip (MS) line. Due to the smaller feature size, 0.1 mm gap, this makes it harder to print reliably. This gap size is critical in order to achieve a characteristic impedance of 50Ω in a CPW, thus an alternative was investigated. Figure 16 shows the dimension of the printed MS lines with signal line, $W = 1$ mm,

$gap = 0.5$ mm, $W_g = 2.5$ mm, and $L_g = 4$ mm. These were printed with the same settings as the CPW and using the same materials.

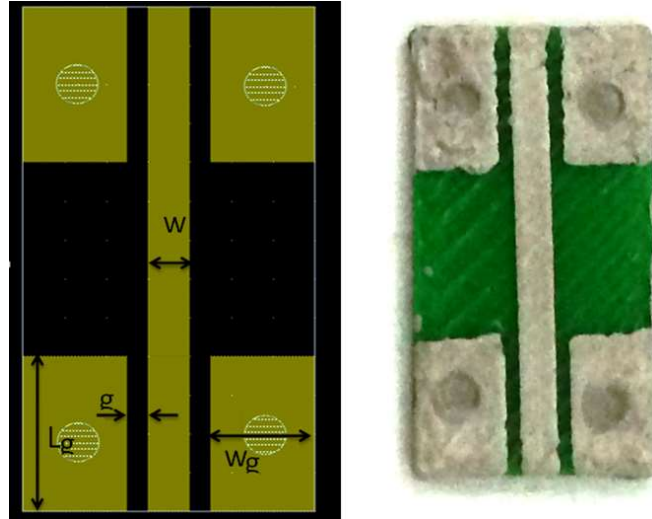


FIGURE 16. DESIGN (LEFT) AND FABRICATED (RIGHT) MICROSTRIP (MS) LINE

WAMI at USF attached the three samples with SMA connectors and were tested with the same procedure as the CPW samples. Figure 17 shows the S-parameters of all three samples made at WAMI at USF.

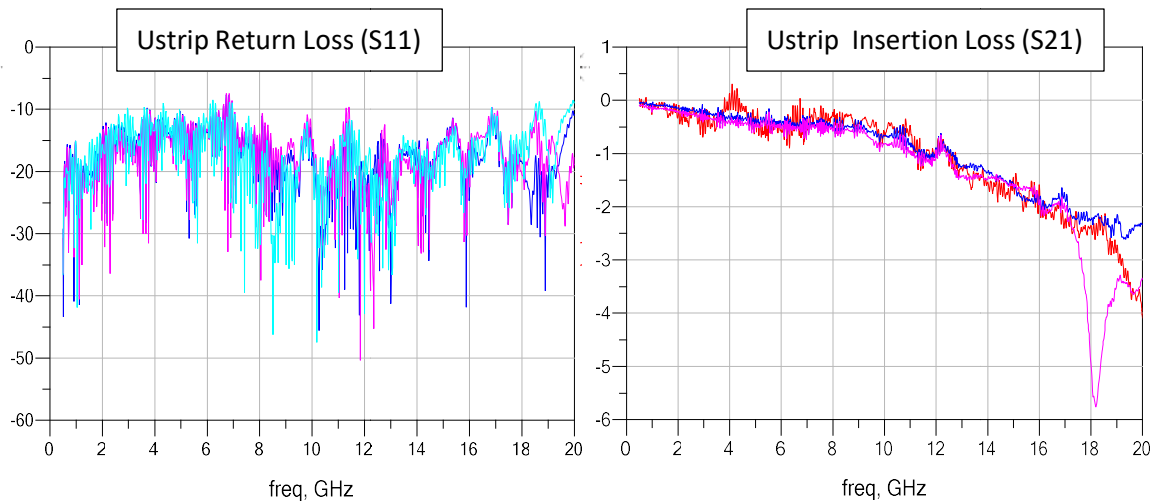


FIGURE 17. WAMI AT USF MEASURED MICROSTRIP LINE DESIGN (LEFT) AND FABRICATED 3D MICROSTRIP LINE ON ABS (RIGHT)

It can be observed that the MS lines perform well up to 12 GHz with losses increasing to over 2 dB at 18 GHz.

Chapter 3: 3D Printed Dual-Channel Antennas

A growing need for long term embedded sensors has seen large investments from a wide range of sources. Many studies focus on low-power wireless sensing with on-board energy harvesting techniques or micro-batteries. In this chapter, a few antennas will be discussed and demonstrate how 3D printing can overcome the challenges with wireless sensing nodes in terms of size, power consumption and communication range.

In this chapter, two dual-channel antenna designs are presented with a progression of complexity in fabrication. In these antennas, ABS parts were printed with commercial tools before the direct write extrusion was performed with the nScript tool. Fiducial marking, print pathing, and conformal printing customization enable the addition of complex antenna designs. Each added complexity shows improvement in electrical performance and packaging efficiency. The first CPA design attempts dual-channel communication with two separate antennas for reception and transmission. The design is simple and demonstrates basic 3D printing techniques to improve a device packaging. The second design is extended into the third dimension in an extreme way while adding electrical function and physically obstructive features. The third design requires DW deposition on both sides of an unstable substrate while conforming to the meandering path and the rough surface, which is characteristic of the slopes of FFF parts. These antennas were designed by Dr Nassar in his dissertation [35].

3.1 3D Printed Dual-Channel Circular Patch Antenna Array with Miniaturization

A dual-channel circular patch antenna (CPA) array is illustrated in Figure 18. Each channel has four circular patch antennas with a 2 by 2 arrangement. The transmitting and receiving circular patch radius, R_1 and R_2 , are 22.5 mm and 11 mm, respectively which are approximately $\lambda_g/4$. The substrate and ground plane radius, R_g , is 80 mm. The distance from the center of the 2.4 GHz and 4.8 GHz patches to the center of the array, X_1 and X_2 , are 50 mm and 30 mm, respectively. The receiving 4.8 GHz antennas and their feeds are rotated 45° to minimize the occupied area and ensure the alignment of the current polarization with the transmission

antennas. The substrate is FFF printed, with a commercial printer, out of ABS with a thickness of 100 mils (2.54 mm) and the patches were DW extruded afterwards with Dupont CB028.

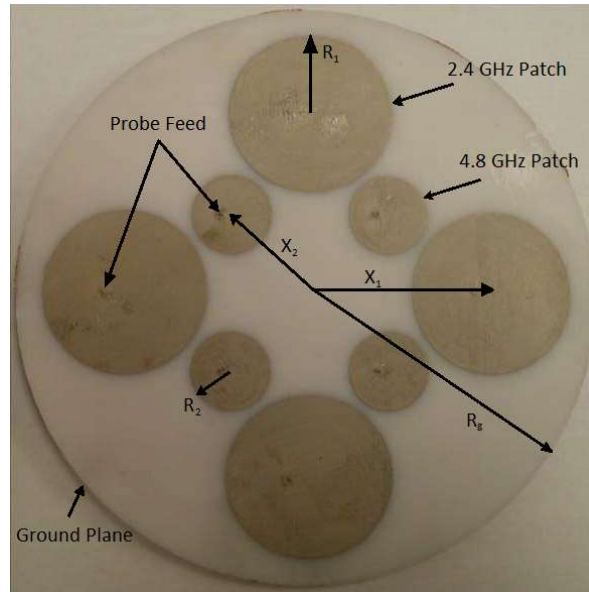


FIGURE 18. FABRICATED DUAL-CHANNEL CIRCULAR PATCH ANTENNA ARRAY

Due to the size and symmetry of the substrate, warping occurred which produced a bow in the printing surface and the shape made it difficult to orientate the substrate to a fixture with a reference direction. The large deposition area also requires a long scan time for conformal printing. To reduce total fabrication time, each patch was printed individually and the probe feed holes were used as fiducial markers to translate and orientate each patch. The 2.4 GHz patches would sometimes have voids during the infill process, due to clogging or air pockets in the syringe. The clogs were resolved by increasing the air pressure to 60 psi during the print and then returned to 10 psi when material flow resumes. Voids were touched up by hand post-print. This was not an issue for the 4.8 GHz patches due to their shorter print time. These were printed with a 0.1 mm valve opening, 20 mm/s print speed and 10 PSI air pressure. After all the patches were printed, they were cured in an oven at 60°C for an hour to dry. The printed CPA had electrical performance comparable to conventionally fabricated one in [36], but it did demonstrate a frequency shift of ~0.2 GHz in the 4.8 GHz antenna.

3.1.1 MINIATURIZATION OF THE CPA

The miniaturization of the size of the CPA is highly desirable for different applications. Inserting slots, loading the patch with shorting pins or using high permittivity substrates and thick multilayer substrates have been done [35]. In this work, a regular CPA and a miniaturized CPA were fabricated and characterized for comparison. The patch was miniaturized by exploiting 3D printing technology in creating arbitrary 3D structures with conformal surfaces. Instead of printing the antenna on a planar substrate, the patch is printed onto a uniaxially varying profile, as shown in Figure 20. Both antennas were designed to operate at 2.3 GHz. The CPA radius is reduced by 14 % compared to the regular patch, as shown in Figure 20.

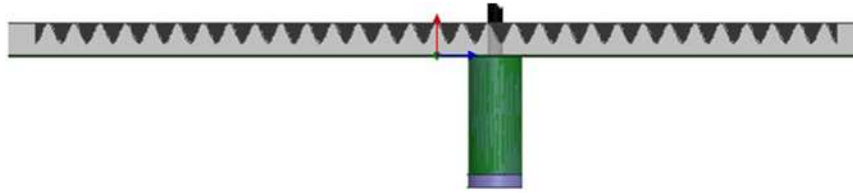


FIGURE 19. SIDE VIEW OF HEIGHT VARYING PROFILE*

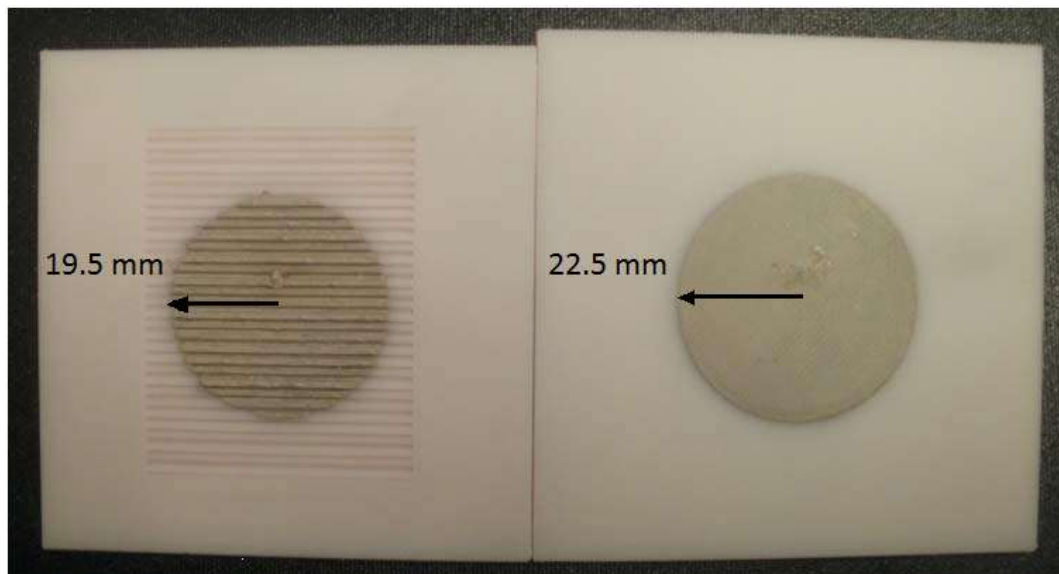


FIGURE 20. SIDE VIEW (TOP) AND TOP VIEW OF THE MINIATURIZED (LEFT) AND PLANAR CPA (RIGHT)

3.1.2 MINIATURIZED CPA FABRICATION

The patch substrate was printed similarly to the previous method. The top surface of the miniaturized substrate was designed by Dr Nassar, to vary height (Z) between 50 and 100 mils, as shown in Eq. (1):

$$Z = 1.5 \times \sin(0.5 \times \pi \times Z) \times \sin(0.5 \times \pi \times Z) \quad (1)$$

Both patches were printed with the nScript 300 tool with a 125/175 μm (ID/OD) nTip, tuned for 0.2 mm width lines. The dispensing gap was set to 50 μm with a printing speed of 20 mm/s for the planar substrate and 10 mm/s for the miniaturized version. A slower speed was necessary to allow the paste to settle for the miniaturized version. No conformal scan was performed due to substrate inaccuracies over the conformal surface.

3.1.3 RESULTS AND CONCLUSION

In total, the whole device weighed 49.5 g before miniaturization. The vertically meandering surface on the substrate reduces the occupied area and weight by 14% at the expense of 2 dB gain degradation and reduction of 0.3% 10 dB return loss bandwidth. This CPA offers the advantages of being low-profile, light-weight, planar and easy to fabricate and integrate. This device also demonstrated that adding a simple variance in the third dimension can improve the packaging of a device without much loss in electrical performance. More detailed results can be found in the dissertation by Nassar [35].

3.2 Quasi-Yagi Dipole Antenna (QYDA) Array

A quasi-Yagi dipole antenna (QYDA) is a uni-planar, unidirectional, resonant type antenna with a compact size and broadband characteristics. It has an endfire radiation pattern and is a suitable element for linear arrays. The drawback of this antenna structure is the required balanced feed and transition to coplanar strips (CPS) which introduce bandwidth limitations [37]. These elements would usually be designed on a 2D plane and take up a large area. In this work, the antenna elements and directors are folded into the third dimension which reduce the 2D footprint but add challenges to the DW method.

3D printing enables metallization on complex structures not previously possible. In this study, a proof-of-concept 3D antenna array, similar to the CPA, is fabricated with extra complexity introduced vertically into the third dimension. Extra functionality can be added within the same floor plan when the antennas rise vertically over the ground. The antenna consists of three parts: a reflector, a driver element, and a director. The width of the director and its distance to the driver element impacts the gain and impedance. This antenna was designed by Dr Nassar in his dissertation [35].

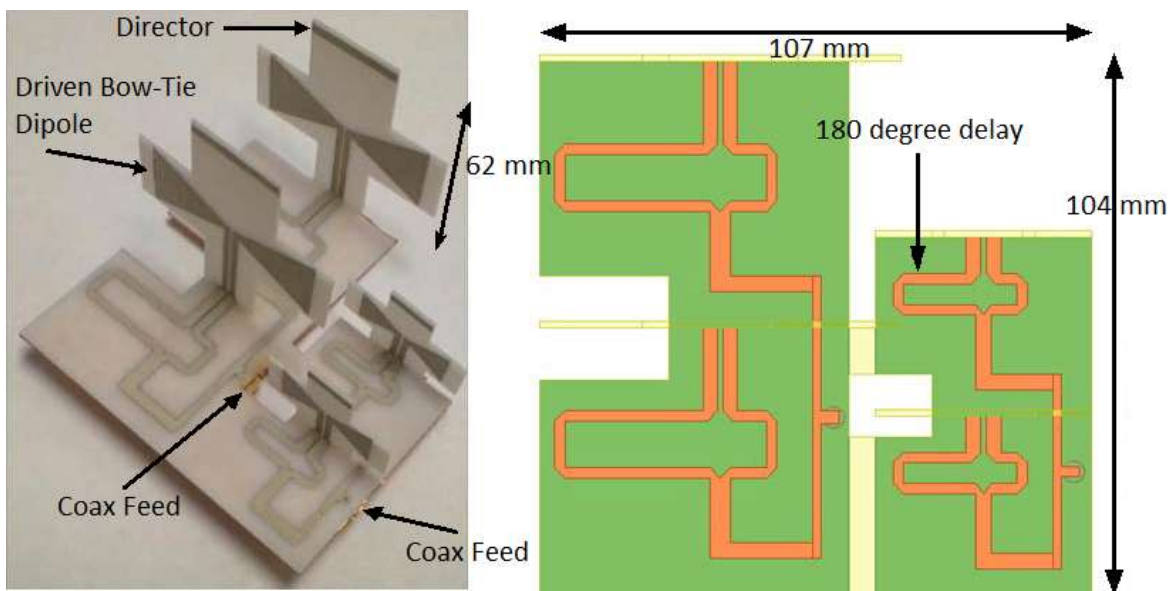


FIGURE 21. FABRICATED QUASI-YAGI DIPOLE ANTENNA ARRAY (LEFT) WITH TOP VIEW OF DESIGN (RIGHT)

Figure 21 illustrates the two-element (2x1) quasi-Yagi dipole antenna array. Compared to the circular patch antenna array, this array has a 3D structure and provides broadband characteristics and endfire radiation. The antenna element consists of a driver, a director, and a broadband microstrip-to-coplanar strip line (CPS) balun backed with a truncated ground plane. The antenna structures were printed with a commercial FFF printer with support structures to allow the fabrication of the overhanging features. The FFF substrate was completed before the DW method is applied. The array is fabricated on a 50 mils ABS substrate with direct write

extruded Dupont CB028 and weighs 16.3 g. The CPA balun was designed away from the high structures to ease DW extrusion.

3.2.1 QYDA FABRICATION

The substrate was separately 3D printed out of ABS before the direct write process. This introduced many challenges into the printing process: varying line width, under-feature printing, and X-Z plane printing.

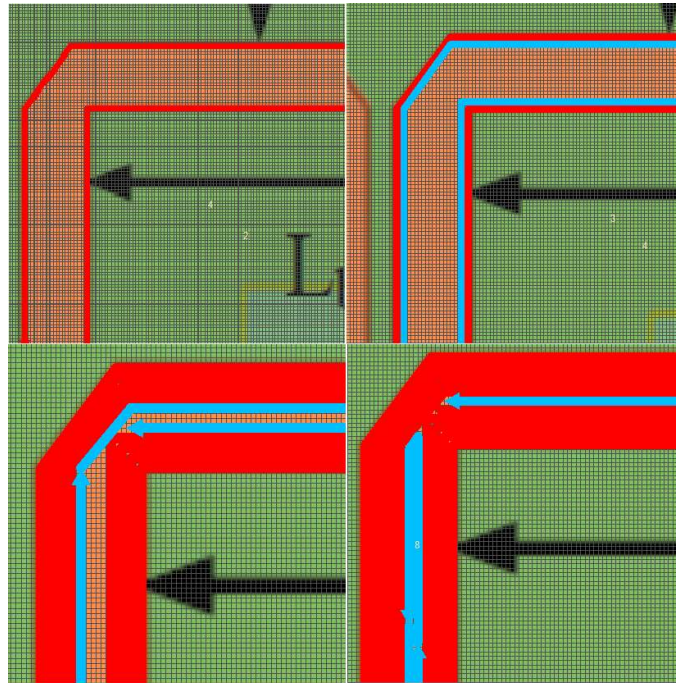


FIGURE 22. PROGRESSION IN PCAD OF LINE FILL ORDER FOR EVEN HOMOGENEOUS FILL FACTOR

Figure 22 illustrates the 200 μm wide-line path to fill the varying width with the same fill factor throughout the trace. A 125/175 μm nTip is initially tuned for 200 μm line widths to match the designed line path. Start and stops need to be tuned correctly to minimize overfill. Figure 22 (top left) is the outline of the trace, this line is offset 100 μm towards the center of the trace to account for accurate trace widths.



FIGURE 23. EFD TIP OPTIONS

The SmartPump's width makes printing near or on tall features difficult due to collisions which can damage the ABS substrate. The nScript SmartPump has multiple tip options, we used a 50.8 mm (2 inch) EFD tip which allows us to print within ~3 mm of the tallest structure. With the nScript nFD pump, we can print modification parts to reach traces which run under the overhanging features. A 45° attachment was printed and added to the SmartPump to access these covered areas. Standard print pathing is designed to end 3 mm before these features, before the attachment is installed and used to connect the traces.

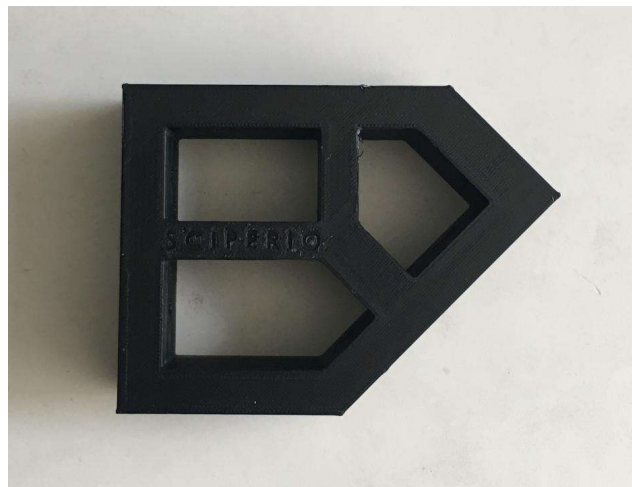


FIGURE 24. 3D PRINTED 45° ATTACHMENT

The vertically standing features also use the 45° attachment and use the bottom left corner of the substrate as a reference point, as shown in Figure 25. The antenna pathing was

designed on the X-Y plane and then the numbers were imported into Excel to convert to X-Z plane. Dry runs were used to account for EFD tip width scraping the bottom substrate and to check for alignment. Visual fiducial marking adds contact on the substrate, which can be undesirable in some situations. Dispense gap was critical to prevent excess build-up of material which would lead to dripping.

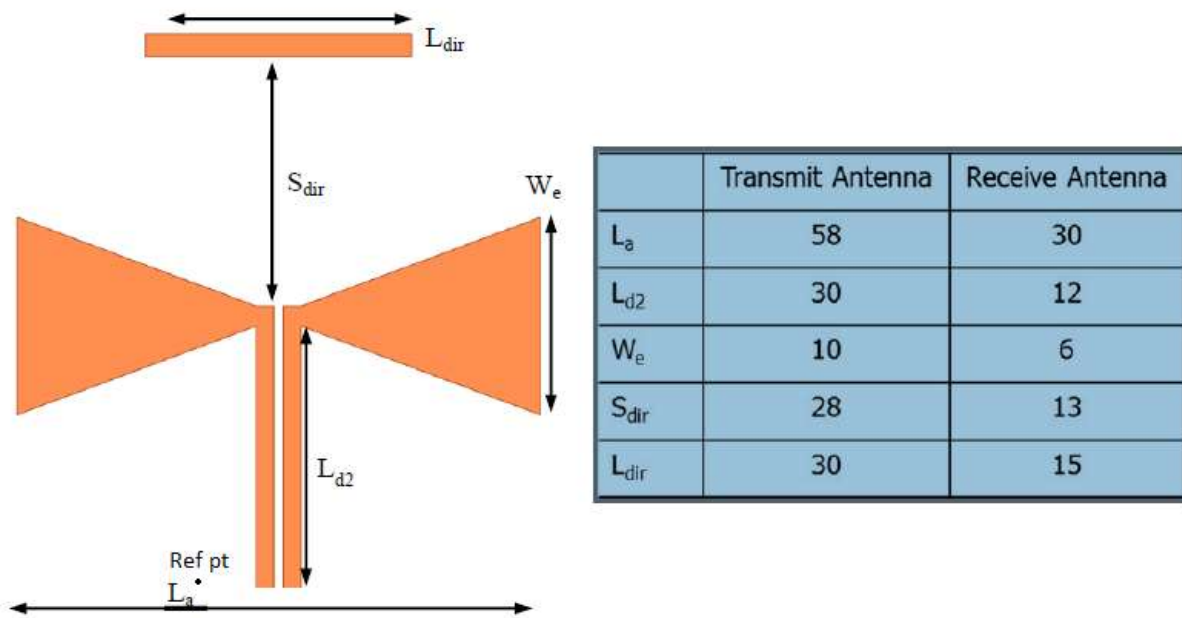


FIGURE 25. DESIGN OF THE QUASI-YAGI ANTENNA WITH DIMENSIONS BY DR NASSAR [35]

3.2.2 Conclusion

Unlike the CPA array, the QYDA array has broadband characteristics but suffers from poor FBR, low gain, and wider beamwidth compared to the size, and the increased design and fabrication complexity. It should be mentioned that simulations of increased number of elements of the array from two to four show a reduced HPBW, however, without a remarkable increase in the peak gain. This is attributed to the relatively wide beamwidth of the antenna element.

The 3D design allowed the addition of a director and the large antennas without increasing the footprint of the design. Using the 3D printed 45° attachment allowed printing onto the X-Z plane while the 3 inch EFD tip allowed printing close to the obstructing features without

collision, and when printing in conjunction with the 45° attachment, allowed printing under the overhanging features. With conventional means, a multi-axis tool would be necessary to print up the X-Z plane and a triple material printing tool would be needed to print conductive traces under an overhanging feature.

3.3 Log-Periodic Dipole Antenna (LPDA) Array

3.3.1 INTRODUCTION

A log-periodic dipole antenna (LPDA) is a classic broadband antenna design used in numerous applications including radar signal detection and radio broadcasting. As a candidate for a dual-channel harmonic interrogator[38], this antenna can provide a bandwidth of 2:1 with persistent radiation pattern. The LPDA has high directivity with low cross-polarization ratio over a wide frequency range.

The LPDA array radiation mechanism is similar to the Yagi-Uda antenna where some dipoles function as the driver, reflector, and director elements depending on the operating frequency and the elements electrical length [39]. The antenna can also be viewed as a series of fed array of parallel dipoles. The length of the longest element determines the lowest frequency and the length of the shortest element determines the upper frequency limit. The gain and bandwidth of the array is mainly determined by the number of dipoles used.

Reducing the LPDA array size and weight has always been of interest and various techniques to minimize the element length have been employed. The antenna size can be reduced by the use of high permittivity material, if the antenna is printed on a dielectric substrate, and by loading the dipoles with lumped reactive elements [40]. Another miniaturization technique has been proposed in [41] based on loading the dipoles with cylindrical hat covers. The most commonly used approach, however, is meandering the dipole length by the introduction of different shapes, such as the Koch-shaped lines [42], rectangular meandering lines [43], and algorithm-generated shapes [44].

In this work, we present a light-weight LPDA array fabricated with 3D printing. Dr Nassar designed the LPDA on Ansoft HFSS and exported the structure as .stl file. The substrate was fabricated with a commercial FFF printer with support material to produce the arms. The dipole length can be reduced by shaping the arms with smooth sinusoidal curves. The complex shape of the substrate creates an unstable base to print from and would normal require a fixture to keep steady. With the DW extrusion method, the tip is contactless and exerts little to no force on the substrate during dispensing. But the extruding tip must maintain a constant small gap from the substrate to control the deposition over the rough surface, and not come into contact with the substrate. This allows printing of a substrate without fixtures or holders and at arbitrary orientations. This form of conformal 3D printing moves away from the planar method of printing and away from the conventional layer by layer method. By following the contours of the substrate, we move into the realm of true 3D printing.

3.3.2 FABRICATION PROCESS

The antenna in Figure 26, the substrate was printed separately with vertically meandering arms designed with a sinusoidal curve, where Z is the height which varies between 0 and 2.5 mm and Y is the distance along the arm, as shown in Eq (2).

$$2.5 \times \sin(0.1 \times \pi \times Y) \times \sin(0.1 \times \pi \times Y) \quad (2)$$

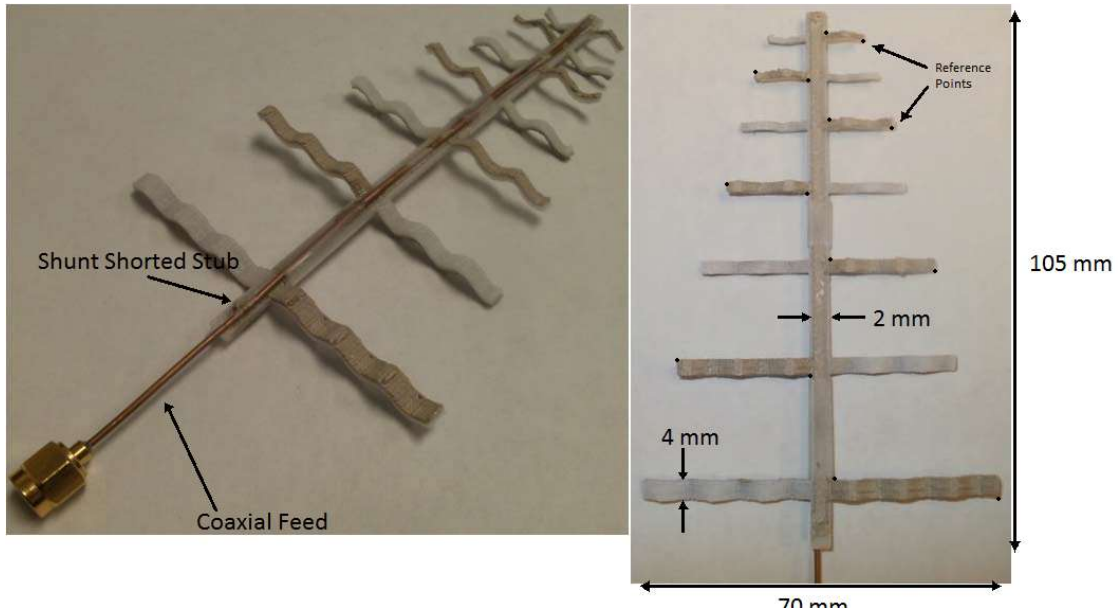


FIGURE 26. TRIMETRIC VIEW (LEFT) AND TOP VIEW (RIGHT) OF 3D PRINTED LPDA ARRAY

These uneven arms require a topographical scan in order to dispense an even layer of CB028. A Z-scan of the arms reveal a surface roughness which could result in the tip colliding with the substrate. Setting the radius cleaning to $300\text{ }\mu\text{m}$, nearly twice the outer diameter of $175\text{ }\mu\text{m}$, ensures no collisions at the cost of increased dispense gap. This trade-off with material control is acceptable since features are much greater than tip diameters, comparing 4 mm with 0.175 mm . Each arm is printed separately with the reference points. The valve opening was set to 0.1 mm with an air pressure of 8 PSI which dispenses a relatively large volume of material which can reach the substrate with a dispensing gap of 0.3 mm . This accounts for the maximum gap from tip to substrate at the steepest slopes of the substrate. Then the print speed was set to 8 mm/s to allow more control and produce a consistent thicker layer of CB028 on top. The coaxial feed was connected with more CB028 and reinforced with scotch tape along the antenna.

3.3.3 RESULTS AND CONCLUSION

The antenna shows good impedance matching over the $2\text{-}7\text{ GHz}$ frequency range. And its gain is similar to the gain expected using a standard LPDA array in [45], however, the bandwidth is improved by 17% . From this study, we can see that simple designs can be printed onto

conformal surfaces without special holders or machined fixtures. While the surface roughness of the LPDA forced a less accurate deposition of CB028, the greatest limiting factor of this printing procedure is the FFF part. Compared to the CPW and MS printed lines, antennas seem to be less sensitive to the roughness of the conductor/dielectric interface.

The 3D printed LPDA array demonstrates wider bandwidth performance improvements compared to its standard counterpart [45] with the added capability to fabricate on-demand designs easily and quickly. It also has reduced weight and size due to the material and the sinusoidal design. In general, electrical performance in the 3D printed antenna matched or exceeded existing designs with further improvements in weight and size.

3.4 Conclusion

In this chapter, two dual-channel harmonic antenna designs are presented. The first CPA array was designed to be low-profile, light weight, planar, easy to fabricate and integrate. This array was minimized by printing the array elements on a vertically-meandering-substrate surface. By using a sine function to vary the height by 50%, the antenna size and weight were reduced by 14% and the gain was reduced by 2 dB. This antenna demonstrated the difference between a conventionally fabricated antenna versus a 3D printed antenna. The different material properties caused a frequency shift and slightly reduced gain, but were still comparable. But the advantage of 3D printing is the added complexity into the third dimension which allowed a reduction in size and weight. The second design of the QYDA allowed us to add a more extreme third dimensional change, which saves space and adds capabilities. This increased the difficulty in fabrication due to the obstructing features. An attachment was 3D printed to add a 45° angle of attach to tackle the X-Z printing and a tip change to an EFD needle which increases the reach of the tip to print onto the substrate without damaging the substrate. The third design of the LPDA allowed the fabrication of a conformally complex design onto both sides of the substrate. The full capabilities of DW printing allowed the part to be printed without the need for fixtures or alignment. Through the fabrication process all of the designs, the greatest limiting factor has

been the surface roughness of the FFF part. DW methods are capable of dispensing onto these surfaces but a smoother surface would provide a great improvement.

Chapter 4: Laser Ablation on Co-Planar Waveguide

4.1 Introduction

Digital AM is showing increased potential for use in microwave/mm-wave circuit and antenna fabrication. The quality and variety of compatible materials are increasing while tool capabilities are expanding. For conductor deposition, direct writing techniques are popular with complementary advantages. Aerosol jetting tends to yield high resolution traces with thin profiles. Aerosol jetting material need to be cured at high temperatures to produce their characteristically high conductive lines. In contrast, extrusion dispensing produces wider lines, $\sim 100\text{ }\mu\text{m}$, but can be cured at much lower temperatures but at reduced conductivity. The DC conductivity of extruded silver paste, Dupont CB028, is $\sim 2\text{MS/m}$ and the effective conductivity can be down to four times lower due to uneven silver flake distribution within the trace path. Dispensing thin traces can produce a tapered profile which further degrades the high frequency performance, especially in coplanar waveguides (CPW) since the currents are confined towards the edges closest to ground. The extruded width and the tolerance affects the reliability of signal-line width and the gap from signal to ground, respectively. These large feature sizes limit the upper frequency range of 3D printed circuits.

In this work, the minimum feature size, tapered profile and silver flake issue are addressed by using a Nd:YAG picosecond laser (Lumera SUPER RAPID-HE) integrated into a nScript 3D printer to machine narrow slots into a layer of micro-dispensed CB028. Laser machining has been used for rapid prototyping of microwave components made with low temperature co-fired ceramics (LTCC), achieving $50\text{ }\mu\text{m}$ and $65\text{ }\mu\text{m}$ wide slots in [46] and [47], respectively. Heat conduction, melting, evaporation and plasma formation occur in short laser pulses according to classic beam-matter interaction, as shown in Figure 27.

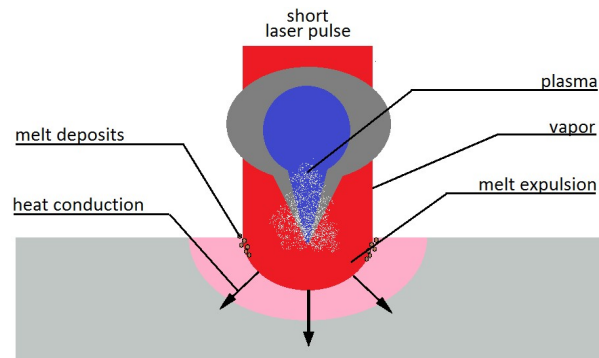


FIGURE 27. CLASSIC BEAM-MATTER INTERACTION

These temperature dependent processes tend to create residual thermal damage, but at even shorter pulses this phenomena is reduced. Due to the emission of very short pulses, the conductor material builds up extreme pressures, densities and temperatures which accelerate the ionized material to enormous velocities. At these ultra-short pulse durations, energy cannot be transferred from the electron gas to the ion grid instantly, the material cannot evaporate continuously but is transferred into a state of overheated liquid, as shown in Figure 28.

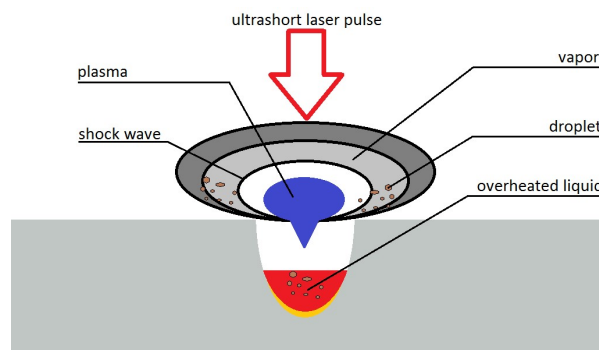


FIGURE 28. ULTRA-SHORT PULSE LASER-MATTER INTERACTION

At nano- and pico-second pulse durations, characteristics of both models can be expected. A finite difference model of the residual thermal conduction, of the laser beam, shows the region of temperatures which exceed the melting temperature of silver, 961 °C [48], as shown in Figure 29.

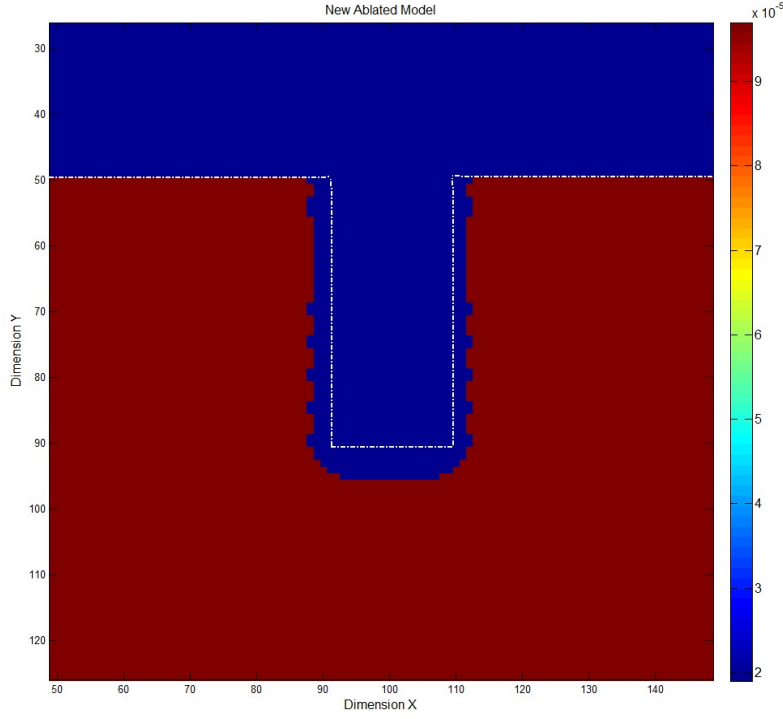


FIGURE 29. LASER ABLATED PROFILE WITH REGIONS OF TEMPERATURES EXCEEDING SINTERING TEMPERATURES OF 1234.15K (961°C)

The red region is the silver paste while the white dotted line is the ablated hole in the silver paste. The blue region within the red represents the regions where temperatures exceed 1234.15 Kelvin. The model from Eq. (6), predicts that a melted region of $2\mu\text{m}$ can be expected after ablation. Residual thermal damage is expected in this area.

The finite difference method was used to calculate the thermal model:

Governing Equation:

$$\frac{\delta T}{\delta t} - \nabla^2 T = 0 \quad (3)$$

Expanding into Cartesian Coordinates

$$\frac{\delta T}{\delta t} = \frac{\delta^2 T}{\delta x^2} + \frac{\delta^2 T}{\delta y^2} \quad (4)$$

Approximate Derivatives with Finite-Difference

$$\frac{T_{i,j}^{new} - T_{i,j}^{old}}{\Delta t} = \frac{T_{i-1,j}^{old} - 2T_{i,j}^{old} + T_{i+1,j}^{old}}{\Delta x^2} + \frac{T_{i-1,j}^{old} - 2T_{i,j}^{old} + T_{i+1,j}^{old}}{\Delta y^2} \quad (5)$$

Where

$$A \equiv \text{Thermal diffusivity area}$$

$$F_0 = \frac{A \cdot \Delta t}{(\min[\Delta x, y\Delta])^2} \equiv \text{Fourier Number}$$

Where the equation is updated to:

$$T_{i,j}^{new} = T_{i,j}^{old} + \Delta t \left(\frac{T_{i-1,j}^{old} - 2T_{i,j}^{old} + T_{i+1,j}^{old}}{\Delta x^2} + \frac{T_{i-1,j}^{old} - 2T_{i,j}^{old} + T_{i+1,j}^{old}}{\Delta y^2} \right) \quad (6)$$

4.2 Laser settings

To characterize the laser, we laser machined ~~many~~ slots in an assortment of samples of CB028 on ABS. The settings of the laser were noted and the samples were viewed under a microscope and optical profilometer to characterize the resulting cuts. Table 3 contains the laser parameters we cycled through and their resultant cut widths observed through a microscope.

Table 3. Laser parameter settings

Repetition Rate (KHz)	Passes	Avg. Power (W)	Pass Profile	Cut Width (microscope) (μm)
250	1	3		32.29
250	1	3		28.42
1000	1	3.9		No cut
100	1	2.4		72.33
50	1	1.93		63.29
10	1	0.74		49.08
10	10	0.74		83.96
10	10	0.74	Going down 500 μm each 5 passes	85.25
10	10	0.74	Going down 100 μm each pass	86.54
10	10	0.74	Going down 50 μm each pass	86.54
100	4	0.74		67.17
100	1	0.74		62
100	2	0.74		59.42
100	10	0.74		83.96
100	20	0.74		73.62
250	1	0.74		60.71
250	2	0.74		72.33
250	5	0.74		64.58
100	1	0.5		15.72

The laser setting with the thinnest width was a rep. rate of 100 kHz and average power of 0.5 W.

4.3 Fabrication Process

A 3.36 mm by 1.5 mm rectangle of Dupont CB028 was dispensed onto a 15 mil-thick Rogers RT5870 substrate using an nScript 3Dn tabletop printer. A 125/175 μm ID/OD nTip was selected and 14 psi back pressure, 20 mm/s head speed, 100 μm print gap, and 0.11 mm valve opening were set to achieve a 200 μm print width. After the design was printed, the samples were cured in an oven at 90 °C for one hour. The repetition rate was set to 100 kHz, peak power to 4 MW, and each slot had 6 passes. This resulted in slot widths ranging between 25 – 40 μm and cut through the 20 – 25 μm thick silver layer. Figure 30 (b) and (c) show the measured profile of the laser machined slots.

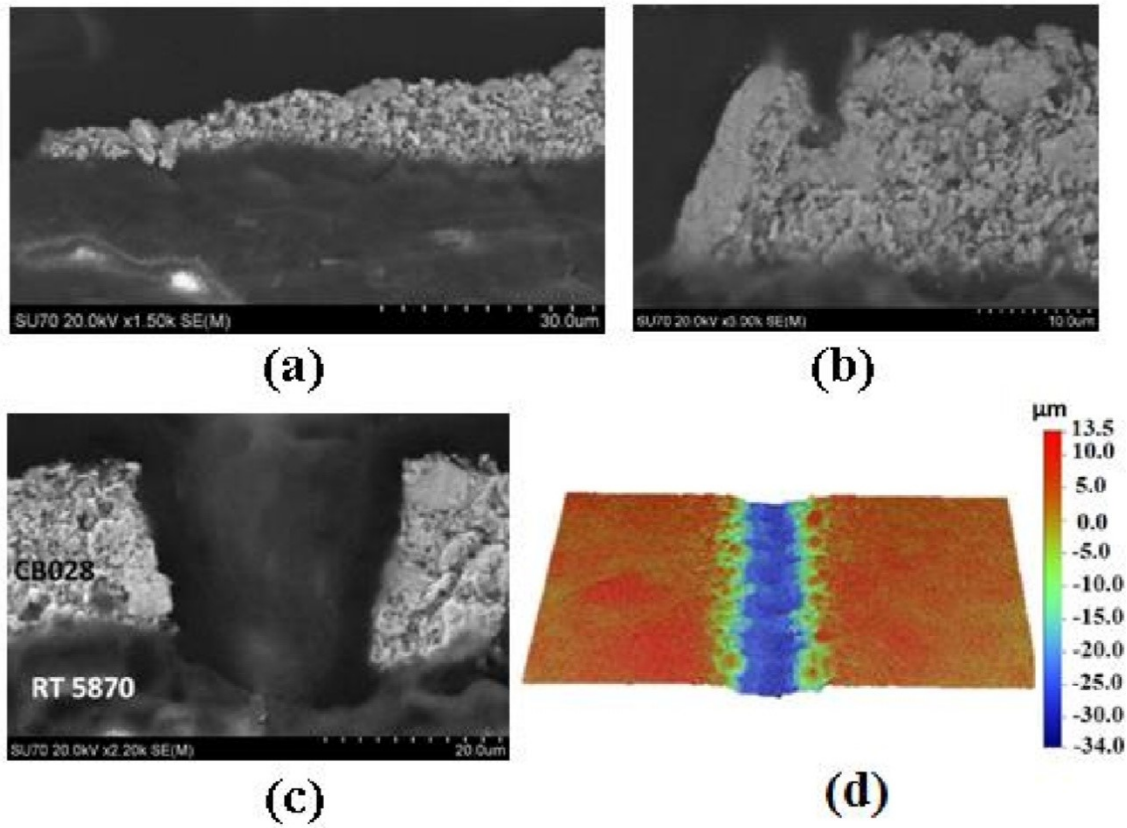


FIGURE 30. A) SEM PERFORMED AT USF OF EDGE OF MICRO-DISPENSED PASTE WITHOUT LASER PROCESSING, B) SEM PERFORMED AT USF OF LASER ABLATED SLOT WITH VISIBLE REGION OF SINTERED SILVER PARTICLES, C) SEM PERFORMED AT USF OF LASER MACHINED SLOT, AND D) 3D PROFILE OF A LASER MACHINED SLOT[49]

4.4 RF Conductivity Measurements

The localized electrical conductivity of the laser-machined CB028 is investigated using the near-field microwave microscopy (NFMM) technique. Details of the design and modeling of the dielectric-resonator based probe are discussed in[50] and[51]. Figure 31 (a) shows a micrograph a sample with 28 μm thick CB028 printed on a RT5870 substrate. A section this sample was laser machined with the previous fabrication process, but using only one pass, to only treat the top layer of CB028 without cutting through. The NFMM measurement is performed at 3 μm above the sample over an area of 260 μm by 15 μm at the intersection between treated and non-treated areas.

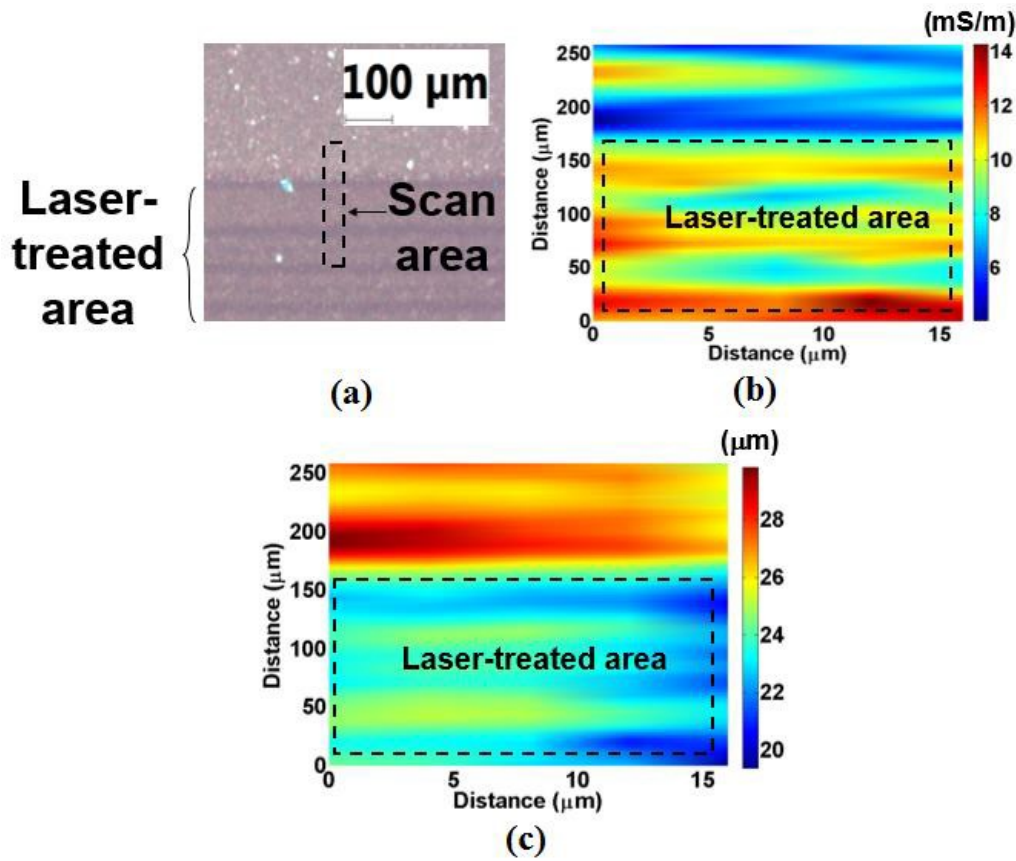


FIGURE 31. (A) MICROGRAPH OF CB028 SHOWING THE LASER-TREATED AREA, (B) ELECTRICAL CONDUCTIVITY OF CB028 FILM USING THE DR-BASED NFMM AND (C) MEASURED SURFACE TOPOGRAPHY[49]

Figure 31 (c) shows the measured surface topography of the CB028. It can be observed that $\sim 5 \mu\text{m}$ of material was removed over the treated area. Bulk silver has a conductivity of 63 MS/m[48] and low temperature cured CB028 has a conductivity of 0.7 MS/m[22]. Figure 31(b) shows conductivity between 10 to 12 MS/m which is over 10 times improvement in conductivity in the laser-treated area over the untreated area. This can be explained by the melting and solidifying of the silver flakes across the surface as a result of the laser treatment.

4.5 Conclusions

Picosecond pulsed laser machining of direct write CB028 paste has been shown to yield high contrast features and solidified silver in a narrow region at the edge of machined areas. This

resulted in a significant increase in the conductivity in these regions. CPW lines with laser machined slots have measured attenuation constants of 0.74 dB/cm (CB028 only) and 0.61 dB/cm (copper plated CB028) at 20 GHz; these values are comparable to those obtained from CPW lines of similar dimensions that are fabricated using copper-clad liquid crystal polymer (LCP) substrates. Moreover, the process described in this work enables the use of direct write extrusion for microwave structures operating up to 40 GHz, due to the reduction of the minimum achievable slot size.

Chapter 5: 3D Printed Multi-Material Broadband Structural Current Sheet Antenna Array

5.1 Introduction

The advances in printing technology, expansion of material options, and greater understanding of the mechanical and electrical properties of the printed structures are all contributing to the potential realization of high performance, 3D printed structural electronics.

The first demonstration of a phased array unit cell fabricated using additive manufacturing was published in 2015 [11] [12]. The design of the unit cell antenna leverages an important capability of DDM in being able to spatially vary the dielectric constant of the constituent substrate layers and the performance was on par with that achievable using low loss, copper-clad microwave laminates. In this chapter, a second example of DDM-produced microwave structural electronics is the broadband 2-18 GHz current sheet antenna (CSA) array as shown in Figure 32.

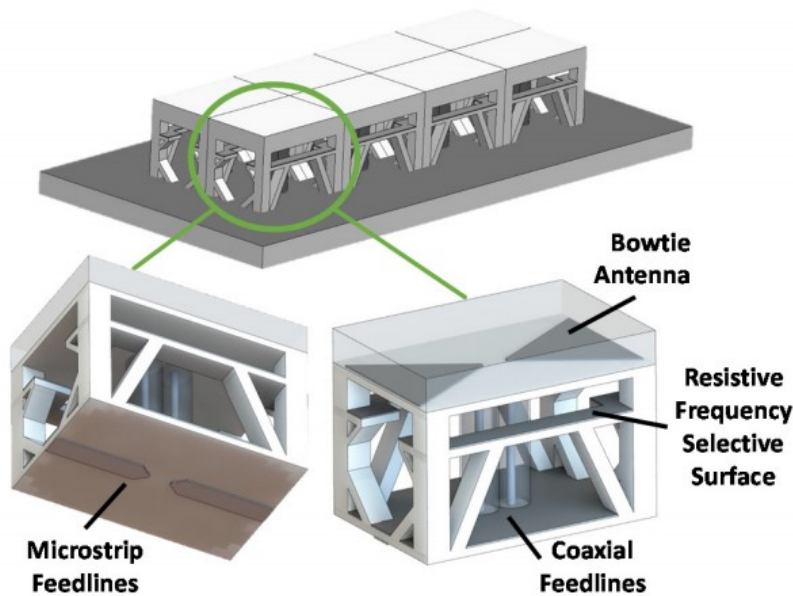


FIGURE 32. 2X4 ELEMENT 2-18 GHz CURRENT SHEET ANTENNA WITH BOTTOM VIEW (LEFT) AND TOP VIEW (RIGHT) OF AN INDIVIDUAL UNIT CELL

This structure has been developed using the same additive manufacturing technique as the 2.45 GHz array, but with a focus on joint electrical-mechanical design practices. In particular, there was an emphasis on characterizing the mechanical and electrical properties of the printing material when subjected to external forces and changing environmental conditions. Antennas with multi-octave bandwidth are especially useful in applications such as wideband radar and signal identification systems. The array of strongly coupled antenna elements or unit cells [44] and generally requires a 3D architecture. In this work, each unit cell consists of a differentially fed bow-tie antenna on the top of the substrate with a vertical dual coaxial transmission line feed structure that connects the antenna to the microstrip feed lines on the bottoms of the substrate. To achieve extremely broadband operations, the addition of a resistive frequency selective surface (FSS) in between the antenna elements and the array ground layer is required [45]. Structural electronics may introduce new challenges in meeting environmental requirements like temperature, humidity, and vibrations. Reliability under the environmental stresses depends on parameters such as adhesion between conductor and dielectrics, thermal expansion differences, and the material stiffness.

5.2 Initial Design

A study was conducted on the antenna element, a 2 GHz bowtie box design was fabricated with ABS. The substrates were printed with a 125/175 μm ID/OD nTip, set to 200 μm extrusion width and 50 μm layer thickness, with 5 shells and 5 solid top and bottom layers. Substrates were printed before being removed for direct write printing of DuPont CB028 for the bowtie and ground plane. Warping and cracking were observed and adjusting bed temperature, tip temperature and fan settings could not resolve these issues. A redesign for 4 GHz allowed for all dimensions to be halved and no warping or cracking was further observed, as shown in Figure 33.

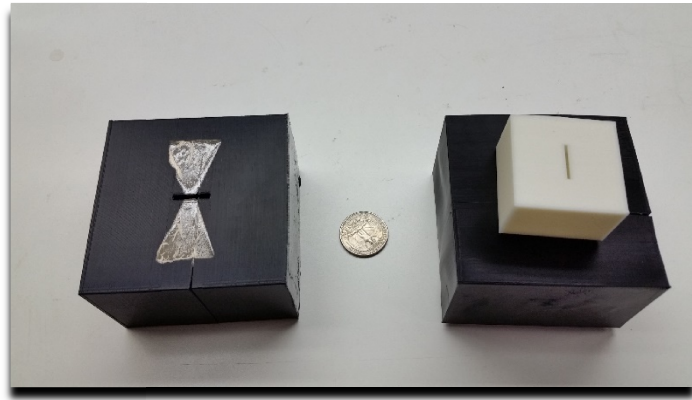


FIGURE 33. COMPARISON OF FABRICATION TOLERANCES OF 4 GHz DESIGN (WHITE) WITH 2 GHz (BLACK).

From the previous study, we could produce hollow structures with overhanging surfaces without support structures with smooth surfaces on all the faces. FFF parameters set to produce test pieces that could be used to characterize the antenna element. These parts were fabricated in two parts, the top substrate which has the antenna element and the bottom which may or may not have a ground layer. . DuPont 7082 is a carbon conductive paste that is used as a polymer thick film resistor with a sheet resistivity of $400 \Omega/\text{sq}/\text{mil}$. This was dispensed into a $200 \mu\text{m}$ void within the FSS shells and cured in the oven at 60°C for 30 minutes to dry before being attached to its bottom ground plane counterpart. These two parts are then adhered to each other by acetone and compared with a conventionally fabricated microstrip bowtie antenna, built with Rogers 4003 and copper-milled by WAMI at USF. Figure 34 shows the fabricated antennas.

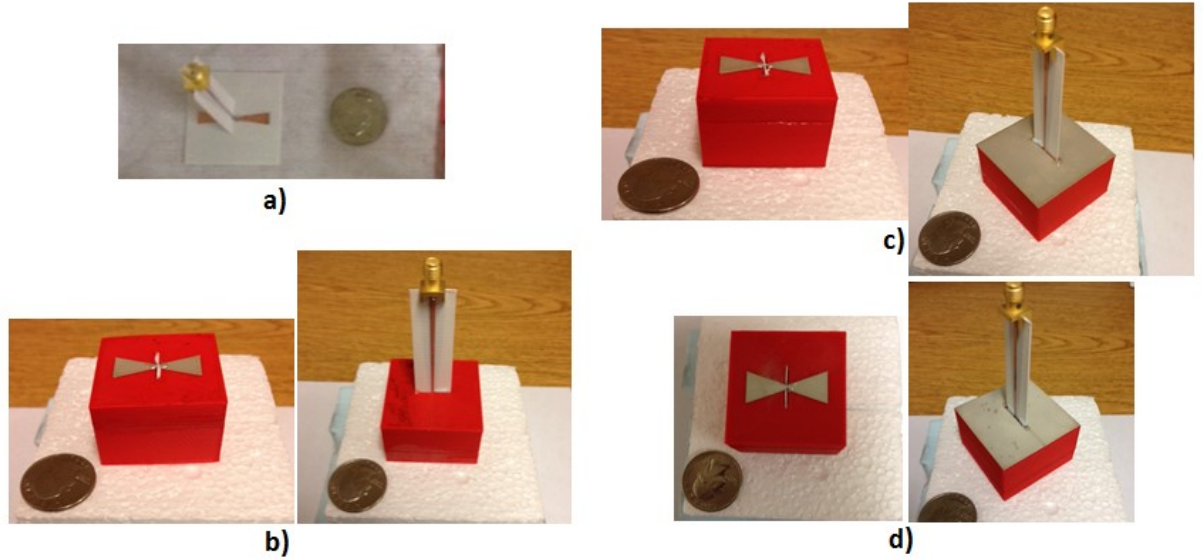


FIGURE 34. BALUN-FED 4 GHz ANTENNA DESIGNS A) CONVENTIONAL MICROSTRIP B) 3D PRINTED WITHOUT GROUND PLANE C) 3D PRINTED WITH GROUND PLANE D) 3D PRINTED WITH FSS RING AND GROUND PLANE

The radiation and gain patterns were similar to the conventionally fabricated device with a small frequency shift. The antenna with the FSS ring did not show any increase in bandwidth, probably due to the resistivity of the of the carbon paste having deteriorated since it had passed its shelf-life.

5.3 FFF Printability of the Unit Cell

The structure of the unit cell was printed with ABS and metalized with DuPont CB028. Hollow high-aspect ratio cylinders were printed with different diameters and extrusion widths. Figure shows a set of 4 mm outer diameter (OD) and 1 mm inner diameter (ID) holes with a set of 2 mm OD and 0.5 mm ID coaxes. Coaxes are 15 mm in height and printed with layer thickness of 0.15 mm which resulted in rough outer and inner surfaces. These samples were printed with a 125/175 μm nTip and the print speed was set to 8 mm /s to reduce the force exerted on the structure while reducing the contact time between the heated tip and the part.

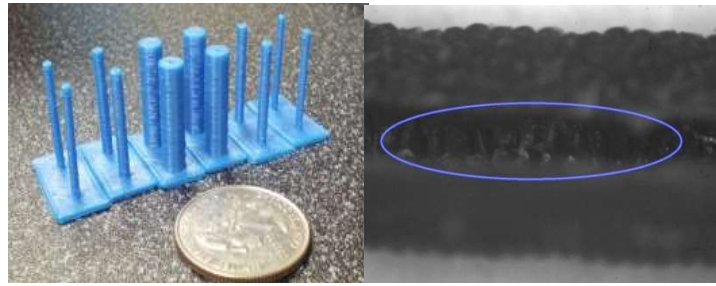


FIGURE 35. 3D PRINTED COAX STRUCTURES (LEFT) WITH OPTICAL MICROSCOPIC VIEW OF INNER ROUGHNESS (RIGHT)

During the printing at 235 °C tip temperature, molten plastic would seal the inner diameter and thus failing the print. To prevent this, the tip temperature was reduced to 230 °C and a fan was directed towards the printing area. This rapidly cooled and solidified the extruded plastic. Printing to a height of 15 mm was easily achieved with the 2 mm OD coaxes. Through the parameters found through this study, 2 mm OD and 0.5 mm ID coaxes were fabricated into a unit cell. The resultant unit cell is shown in Figure 36. To keep the top surface smooth, extra layers were added and sloped outwards to keep the corners supported. This doubled the thickness of the top layer and added extra weight to the structure.



FIGURE 36. 3D PRINTED UNIT CELL WITH SAGGING AND CURLED EDGES ON TOP SUBSTRATE.

These initial unit cells had the edges on the top substrate curl up due to temperature gradients in the plastic on the top cooling faster than the plastic below. To remedy this, the bed temperature was increased from 90 °C to 100 °C. This increases the ambient temperature towards

the top reducing warping issues. But this causes extra sagging on the over-hanging layers. A heated box fan was used to minimize this issue as well as the use of support beams. There was a great difficulty printing the bridge feature without increasing the thickness of the bridge. Since the top of the bridge had to be smooth and solid, extra layers would usually be required to remedy this issue. Due to the thickness requirements of the bridge to remain at 0.3 mm, the only remedy would be to increase the printing resolution and use layer thicknesses of 0.05 mm. This doubled the number of layers to six from three, which allowed a solid path to be fabricated. This also allowed the top surface to be printed without the extra thickness previously added. Unfortunately, this also doubled the time needed to fabricate the part. This results in an 8 hour printing time for one unit cell. The results of these parameter changes are shown in Figure 37.

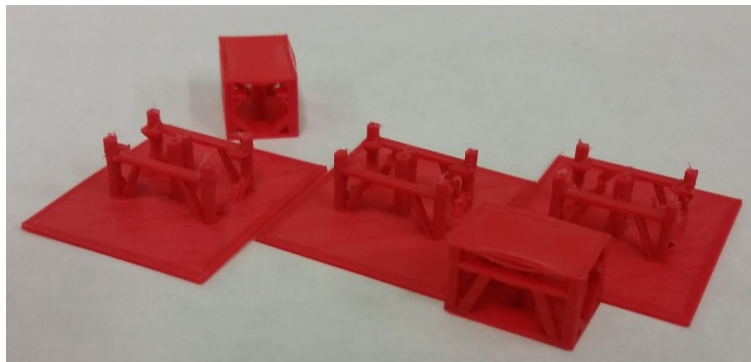


FIGURE 37.FINAL UNIT CELLS WITH FSS RING

Note that the parts in Figure 37 have reinforcement trusses different from the one designed in 5.4 and this will be addressed in 5.5

Electrical Design and Fabrication

5.4 ARRAY MECHANICAL REINFORCEMENT

Compression tests were carried out on four antennas in a 2x2 array. The arrays contained the structural material but no electrical features. Each test piece was a 2x2 array of the basic antenna elements. To test layer thickness effects, two antenna arrays were printed with 200 μm layer thickness, one with 150 μm layer thickness and one with 100 μm layer thickness. The two antennas which had 200 μm layer heights had some voids in the planar region near the center

posts. This could have led to a lower compressive force. The 2x2 arrays are able to withstand peak values of 330 – 475 lbf before failure. The thinnest layer thickness produces the most robust results (peak force of 475 lbf) for transverse compression tests. This may be contributed to repeatable and reliable printing rather than the increased lamination contact area.

Further test pieces were printed. For longitudinal tests, a 1x3 array was printed with extra testing attachments on both sides, as shown in Figure 38.



FIGURE 38. 1X3 ARRAY OF UNIT CELLS PRINTED FOR MECHANICAL TESTING

These subsequent test pieces were printed with 50 μm layer thickness. The testing attachment helps connect the 1x3 array to a holder for the longitudinal tests without adding concentrations of force to the overall structure. These tests yielded results with low compression values. The cell was redesigned with reinforcement support beams, as shown in Figure 39. The modified unit cell consists of opposing reinforcing diagonals acting along the front and back faces of the unit cell. The beams were 1 mm wide and 0.5 mm thick. The leaning angle was kept less than 45° to ensure no support material would be needed.



FIGURE 39. REINFORCED 1X3 ARRAY FOR LONGITUDINAL TESTING

This modified design with trusses enhanced the strength-to-weight ratio with a minimal weight increase. The reinforced unit cell has an additional mass of just 7% but greatly increases the longitudinal compressive strength by an additional 150% with an insignificant impact on the electrical performance.

5.5 Electrical Design and Fabrication

Unit cells from Figure 36 were used to characterize the electrical properties and the printability of the electrical features. CB028 lines were printed on the bottom and top of the unit cell. On the bottom, lines were printed from the coaxial holes to their opposite edges. On top, the two coaxial holes were connected with a single trace. CB028 was then injected through the coaxes to connect the two sides and then cured on its side at 60°C for 1 hour. Multiple cycles of injecting and re-curing could not produce a reliable connection through the coaxial feature. Repeatable conductivity could not be obtained and a 0.5 mm diameter copper wire was cut to 10 mm length and was inserted instead and connected with CB028 to the conductive traces. The CB028 acted as an epoxy and connection for the coaxial-to-line transition and were tested, as shown in Figure 40. The copper wire provided much better conductivity than the CB028 within the coax and eliminated the poor conductor/dielectric interface found with the CB028 on ABS. This was a great factor to the performance of the unit cell since the conductivity within the coax would have been too low.

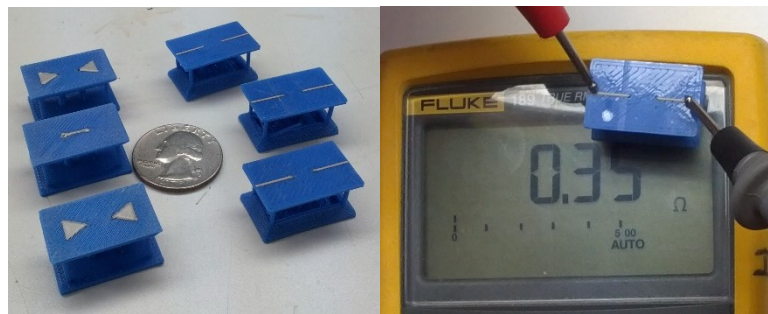


FIGURE 40. UNIT CELL PRINTS OF BOWTIE AND COAXIAL TRANSITION (LEFT) TOPSIDE ON THE LEFT WITH BOTTOM SIDE ON THE RIGHT WITH CONDUCTIVITY CHECK PERFORMED WITH A MULTIMETER (RIGHT)

Unit cells with the printing parameters from Figure 37 were used for the fabrication of high frequency test pieces. These parts were flat on the top and bottom and could be easily aligned on the bed. The extrusion tip was visually brought to the surface of the substrate before being raised to achieve a 50 μm dispensing gap. The 125/175 μm nTip was tuned to print 0.2 mm wide traces and adjusted for pen tip width. Start and stops occurred at the coaxial hole so

minimize the effects of the build-up of material at those points. Printing on the outer surface of the coaxial features would not be feasible with the 45° attachment used in a previous chapter. Thus, the outer diameter was sprayed with CB028. A commercially available air brush was used. The CB028 was stirred with Dupont 3610 at a 1:1 ratio by volume, this was then transferred to the air brush paint bottle and shaken with the lid on. This lowered the viscosity of CB028 and produced a more even distribution of silver particles when sprayed. The air brush was directed between the outer support beams and used to coat the outer surface of the coax features with CB028. The close proximity of the air brush produced areas of high concentration of silver particles and areas with low concentration of silver particles. These parts were then cured in an oven at 60°C for an hour. SMA connectors were attached and tested by WAMI at USF. The parts with SMA connectors attached are shown in Figure 41.



FIGURE 41. TOP VIEW (LEFT) AND BOTTOM VIEW (RIGHT) OF THE COAXIAL TRANSITION TEST COUPONS WITH TUNED PRINTING PARAMETERS. SMA CONNECTORS WERE ATTACHED FOR RF MEASUREMENTS.

The test coupons performed as simulated up to 14 GHz. Higher frequency performance degradation is suspected to be caused by insufficient coverage of CB028 on the outside of the coaxes, or ground plane resonance, or the quality of the SMA connectors.

In order to produce an even distribution of silver particles onto the outer surface of the coax feature, a further spraying distance would be required and additional coats were added. To facilitate this, the unit cell was printed in parts. The base and coaxes would be printed and then

sprayed before the support and FSS structures are attached with the final top antenna pieces. The unit cell is separated as shown in Figure 42.

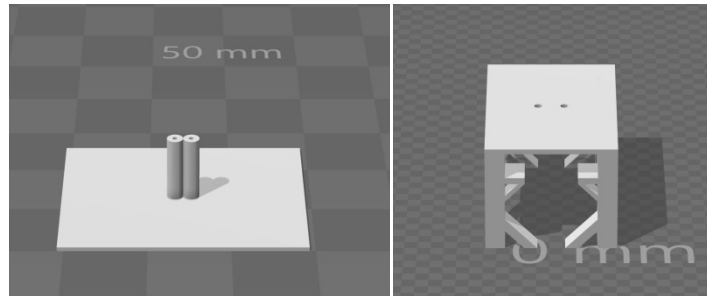


FIGURE 42. UNIT CELL SEPARATED FOR MODULAR PRINTING BOTTOM WITH COAXES (LEFT) AND FSS WITH TOP SUBSTRATE (RIGHT)

The bottom substrate sprayed with three coats and is cured at 60°C for 1hr. The top substrate is built up to before the top substrate is printed, then the tool switches to DW extrusion. Dupont 7082 is extruded onto the bridging area. Figure 43 demonstrates the FSS layer extrusion process on a 2x4 array. The fiducial markers are located at the corners of the FSS bridges and the pen tip does not physically touch the protruding features on top.

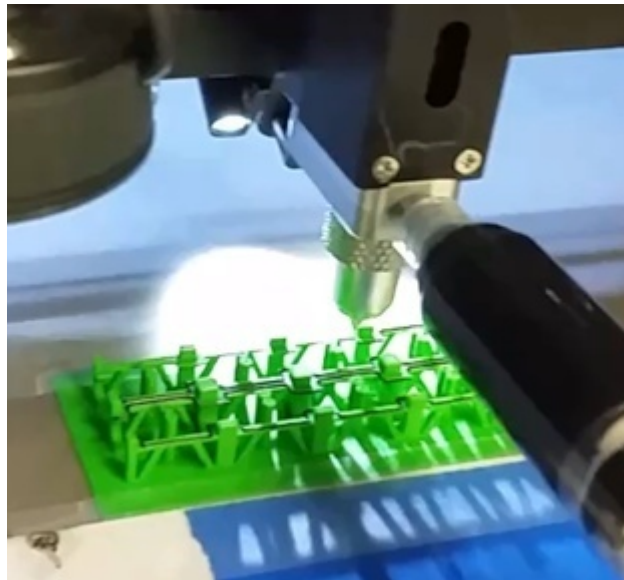


FIGURE 43. DW EXTRUSION PROCESS OF FSS LAYER ON 2x4 ARRAY

In order to attach the top substrate to the bottom, a mixture of acetone and dissolved ABS is lightly applied to the CB028 layer of the bottom substrate. This is left to dry to create a thin layer of ABS on top of the CB028. This creates a layer for the top substrate to adhere to. Acetone is applied to the coax-to-top substrate interface and to the support-to-bottom substrate interface before they are brought together and held for 30 seconds to dry and set. No excess force to push them together is applied as that would force some semi-dissolved plastic out and change the total height.

5.6 FINAL UNIT CELL ANTENNA

Final unit cell samples were printed with all the previous adjustments and WAMI at USF attach higher rated SMA connectors, as shown in Figure 44. These test samples are identical in dimensions to the unit cells from Figure 41, but the top layer microstrip line was removed and the bowtie antenna element was printed on the top substrate.

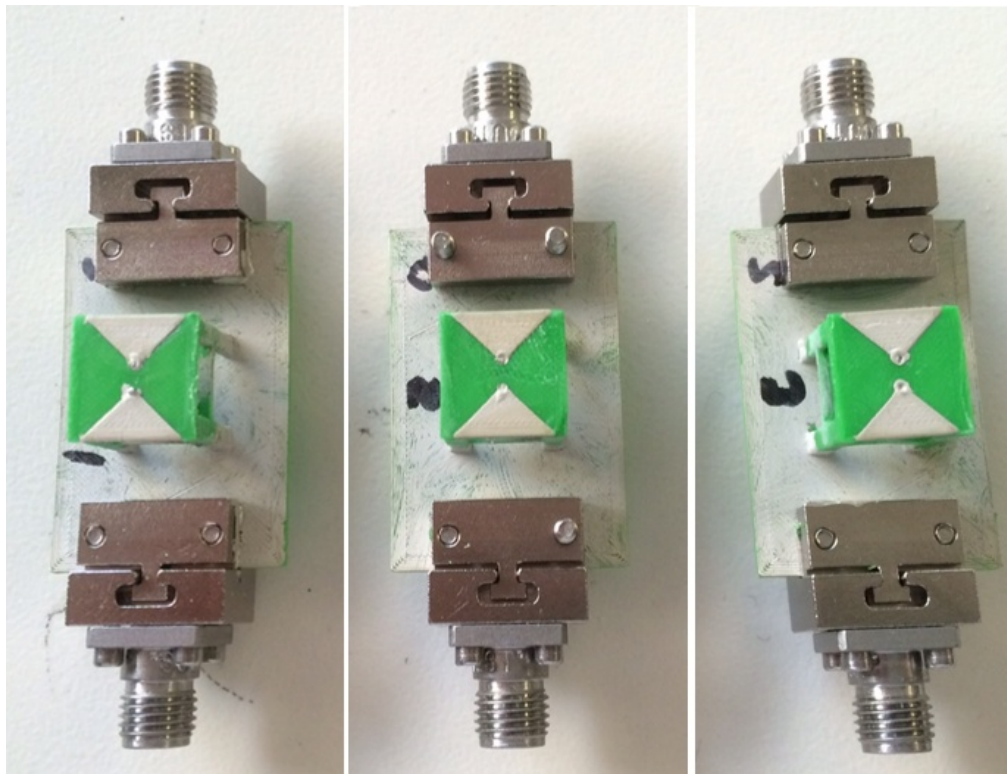


FIGURE 44. 3D PRINTED UNIT CELL ANTENNA TEST SAMPLES

These unit cells measured data closely matched the simulated data with 3-5 dB reduction above 5 GHz. A resonance was observed at around 14.5 GHz which was not in the simulated data. This could be due to the height of the unit cell deviating from the design during the fabrication process. The design can be adjusted to account for this fabrication tolerance and push the resonance frequency above the 2-18 GHz bandwidth.

5.5 Conclusion

One of the strengths of 3D printing in creating structural electronics is the capacity to create 3D geometries that are not feasible with traditional manufacturing methods. This design freedom can be used to optimize weight/strength tradeoffs. 3D printed materials are electrically and mechanically viable for the use in structural electronics and have been demonstrated in this study. As new 3D-compatible materials are developed, and even as the use of existing materials expands into new application domains, an enhanced understanding of structural properties becomes critical. In this study, we examined the structural, electrical and environmental effects of 3D printed antenna arrays. Even though, the common 3D printed materials are more brittle, due to small defects and voids in the printed parts and weaker bonding between layers, we have demonstrated comparable antenna array performance to conventionally manufactured versions.

Chapter 6: Summary and Recommendations for Future Work

6.1 Summary

Chapter 3: 3D Printed Dual-Channel Antennas has demonstrated the viability of commercial FFF and novel DW fabrication techniques. Using improved pathing, angled attachments and alternate tips, the DW process can dispense onto many type of FFF surfaces. It is possible to start moving away from the conventional 2.5D form of layering and convert to a fully 3D fabrication method. The electrical performance of 3D printed antenna devices is comparable to conventionally fabricated parts while also reducing the weight and size of the total package. The drawback of commercially printed FFF parts are the rough surfaces which make the DW process difficult and can reduce the high frequency electrical performance of devices.

Chapter 4: Laser Ablation on Co-Planar Waveguide introduces a new digital process which significantly improved the electrical conductivity of 3D printed conductive materials. This process does not damage the substrate underneath and is easily integrated into the 3D fabrication process. High frequency performance above 40 GHz can be realized in 3D printed devices with standard printed materials. Chapter 5: 3D Printed Multi-Material Broadband Structural Current Sheet Antenna Array uses high resolution FFF printing to minimize the surface roughness observed in Chapter 3: 3D Printed Dual-Channel Antennas and the parameters are tuned to also minimize warping and improve layer adhesion in the FFF part. In this chapter, modular printing and hybrid processes allow a multi-material antenna array to be fabricated to demonstrate a 3D printed structural electronic.

6.2 Recommendations for Future Work

To enable a fully automated hybrid printer, the contraction of ABS at different temperatures would need to be characterized to predict printing heights without the need for a surface scan, thereby reducing fabrication times. Along this line, a study on variable layer thicknesses would further speed up fabrication time in FFF parts.

A further study on the laser could yield settings where only melting would occur and improve the conductivity over a large area without damaging the substrate underneath.

References

- [1] “Wohlers Report 2016.”
- [2] W. R. P. Jr and D. T. Smith, “Smoothing method for layered deposition modeling,” US8123999 B2, 28-Feb-2012.
- [3] C. Barnatt, *3D Printing*, 2nd ed. 2014.
- [4] “Slic3r - G-code generator for 3D printers.” [Online]. Available: <http://slic3r.org/>. [Accessed: 28-Nov-2016].
- [5] “FFF vs. SLA vs. SLS - 3D Printing,” *SD3D Printing*, 29-Aug-2013. .
- [6] “Dielectric Constant, Strength, & Loss Tangent - RF Cafe.” [Online]. Available: <http://www.rfcafe.com/references/electrical/dielectric-constants-strengths.htm>. [Accessed: 18-Jun-2015].
- [7] “Mercedes-Benz Trucks uses pioneering future technology: 3D printing: truck spare parts available on demand,” *marsMediaSite*. [Online]. Available: <http://media.daimler.com/marsMediaSite/en/instance/ko/Mercedes-Benz-Trucks-uses-pioneering-future-technology-3D-pr.xhtml?oid=12788778>. [Accessed: 26-Oct-2016].
- [8] R. Borison, 2014 Sep. 2, 266 8, and 1, “All The Ways Your Kids Can Now Customize Their Toys,” *Business Insider*. [Online]. Available: <http://www.businessinsider.com/3d-printing-toys-2014-8>. [Accessed: 26-Oct-2016].
- [9] J. Harbaugh, “Space Station 3-D Printer Builds Ratchet Wrench To Complete First Phas,” *NASA*, 18-Mar-2015. [Online]. Available: http://www.nasa.gov/mission_pages/station/research/news/3Dratchet_wrench. [Accessed: 26-Oct-2016].
- [10] K. K. B. Hon, L. Li, and I. M. Hutchings, “Direct writing technology—Advances and developments,” *CIRP Ann. - Manuf. Technol.*, vol. 57, no. 2, pp. 601–620, 2008.
- [11] “Stereolithography (SLA).” [Online]. Available: <https://www.solidconcepts.com/technologies/stereolithography-sla/>.
- [12] P. I. Deffenbaugh, R. C. Rumpf, and K. H. Church, “Broadband Microwave Frequency Characterization of 3-D Printed Materials,” *IEEE Trans. Compon. Packag. Manuf. Technol.*, vol. 3, no. 12, pp. 2147–2155, Dec. 2013.
- [13] S. S. Crump, “Apparatus and method for creating three-dimensional objects,” US5121329 A, 09-Jun-1992.
- [14] “AJ_Materials_FAQs_DS_v3.pdf.” .
- [15] “CB028.pdf.” .
- [16] “New filament is 1,000 times more conductive than existing filaments on the market,” *3ders.org*. [Online]. Available: <http://www.3ders.org/articles/20150521-new-filament-is-1000-times-more-conductive-than-existing-filaments-on-the-market.html>. [Accessed: 10-Dec-2016].
- [17] admin, “Aerosol Inks,” 10-Mar-2016. [Online]. Available: [/products/metalon-inks/aerosol](#). [Accessed: 10-Dec-2016].
- [18] O. Marketing, “Aerosol Jet Technology,” *Optomec Additive Manufacturing*. .
- [19] “Metalon_HPS-108AE1_v1.pdf.” .
- [20] “Conductive PLA,” *ProtoPlant, makers of Proto-pasta*. [Online]. Available: <https://www.proto-pasta.com/pages/conductive-pla>. [Accessed: 10-Dec-2016].
- [21] “ME101.pdf.” .

- [22] D. A. Roberson, R. B. Wicker, L. E. Murr, K. Church, and E. MacDonald, "Microstructural and Process Characterization of Conductive Traces Printed from Ag Particulate Inks," *Materials*, vol. 4, no. 6, pp. 963–979, May 2011.
- [23] "Metalon HPS-021LV_3340 2b2.pdf." .
- [24] L. Mortara, J. Hughes, P. S. Ramsundar, F. Livesey, and D. R. Probert, "Proposed classification scheme for direct writing technologies," *Rapid Prototyp. J.*, vol. 15, no. 4, pp. 299–309, Jul. 2009.
- [25] "Combining additive manufacturing and direct write for integrated electronics - A review." [Online]. Available: https://www.researchgate.net/publication/288185339_Combining_additive_manufacturing_and_direct_write_for_integrated_electronics_-_A_review. [Accessed: 26-Oct-2016].
- [26] S. L. Merilampi, T. Björninen, A. Vuorimäki, L. Ukkonen, P. Ruuskanen, and L. Sydänheimo, "The Effect of Conductive Ink Layer Thickness on the Functioning of Printed UHF RFID Antennas," *ResearchGate*, vol. 98, no. 9, pp. 1610–1619, Oct. 2010.
- [27] "Hybrid manufacturing: Integrating direct write and stereolithography." [Online]. Available: https://www.researchgate.net/publication/267997833_Hybrid_manufacturing_Integrating_direct_write_and_stereolithography. [Accessed: 26-Oct-2016].
- [28] "nScript-SmartPump-100-Gen2-Brochure.pdf." .
- [29] P. Deffenbaugh, "3D PRINTED ELECTROMAGNETIC TRANSMISSION AND ELECTRONIC STRUCTURES FABRICATED ON A SINGLE PLATFORM USING ADVANCED PROCESS INTEGRATION TECHNIQUES," University of Texas at El Paso.
- [30] B. Li, P. A. Clark, and K. H. Church, "Robust Direct-Write Dispensing Tool and Solutions for Micro/Meso-Scale Manufacturing and Packaging," pp. 715–721, Jan. 2007.
- [31] "ArcCompensation - RepRapWiki." [Online]. Available: <http://reprap.org/wiki/ArcCompensation>. [Accessed: 28-Nov-2016].
- [32] T. Kitazawa and T. Itoh, "Propagation characteristics of coplanar-type transmission lines with lossy media," *IEEE Trans. Microw. Theory Tech.*, vol. 39, no. 10, pp. 1694–1700, Oct. 1991.
- [33] P. I. Deffenbaugh, T. M. Weller, and K. H. Church, "Fabrication and Microwave Characterization of 3-D Printed Transmission Lines," *IEEE Microw. Wirel. Compon. Lett.*, vol. 25, no. 12, pp. 823–825, Dec. 2015.
- [34] K. H. Church *et al.*, "Multi-Material and Multi-Layer Direct Digital Manufacturing of 3D Structural Microwave Electronics," *Proc. IEEE*.
- [35] I. Nassar, "Long-Range, Passive Wireless Monitoring Using Energy-Efficient, Electrically-Small Sensor Nodes and Harmonic Radar Interrogator," *Grad. Theses Diss.*, Jan. 2013.
- [36] B. J. Kwaha, P. Amalu, and O. N. Inyang, "The Circular Microstrip Patch Antenna - Design and Implementation," *IJRRAS*, vol. 8, no. 1, p. 11.
- [37] W. S. Kaswiati and J. Suryana, "Design and realization of planar bow-tie dipole array antenna with dual-polarization at 2.4 GHz frequency for Wi-Fi access point application," 2012, pp. 218–222.
- [38] D. Isbell, "Log periodic dipole arrays," *IRE Trans. Antennas Propag.*, vol. 8, no. 3, pp. 260–267, May 1960.

- [39] J. Yeo and J.-I. Lee, "Planar log-periodic bow-tie dipole array antenna with reduced size and enhanced front-back ratio," *Microw. Opt. Technol. Lett.*, vol. 54, no. 6, pp. 1435–1441, Jun. 2012.
- [40] Y. Zhengguang, S. Donglin, and L. Shanwei, "A novel size-reduced strip line log periodic dipole arrays," in *2005 IEEE International Symposium on Microwave, Antenna, Propagation and EMC Technologies for Wireless Communications*, 2005, vol. 1, p. 56–59 Vol. 1.
- [41] H. Jardon-Aguilar, J. A. Tirado-Mendez, R. Flores-Leal, and R. Linares-Miranda, "Reduced log-periodic dipole antenna using a cylindrical-hat cover," *Antennas Propag. IET Microw.*, vol. 5, no. 14, pp. 1697–1702, Nov. 2011.
- [42] D. E. Anagnostou, J. Papapolymerou, M. M. Tentzeris, and C. G. Christodoulou, "A Printed Log-Periodic Koch-Dipole Array (LPKDA)," *IEEE Antennas Wirel. Propag. Lett.*, vol. 7, pp. 456–460, 2008.
- [43] A. A. Gheethan and D. E. Anagnostou, "Reduced size planar Log-Periodic Dipole Arrays (LPDAs) using rectangular meander line elements," 2008, pp. 1–4.
- [44] M. A. Mangoud, M. A. Aboul-Dahab, A. I. Zaki, and S. E. El-Khamy, "Genetic algorithm design of compressed log periodic dipole array," in *2003 IEEE 46th Midwest Symposium on Circuits and Systems*, 2003, vol. 3, p. 1194–1197 Vol. 3.
- [45] P. Butson and G. Thompson, "A note on the calculation of the gain of log-periodic dipole antennas," *IEEE Trans. Antennas Propag.*, vol. 24, no. 1, pp. 105–106, Jan. 1976.
- [46] M. F. Shafique and I. D. Robertson, "Rapid prototyping of LTCC microwave circuits using laser machining," in *Microwave Symposium Digest, 2009. MTT '09. IEEE MTT-S International*, 2009, pp. 469–472.
- [47] D. M. Nair, W. E. McKinzie, B. A. Thrasher, M. A. Smith, E. D. Hughes, and J. M. Parisi, "A 10 MHz to 100 GHz LTCC CPW-to-stripline vertical transition," in *Microwave Symposium Digest (IMS), 2013 IEEE MTT-S International*, 2013, pp. 1–4.
- [48] "Silver Powder MSDS." [Online]. Available: http://www.saltlakemetals.com/MSDS_Silver_Powder.htm. [Accessed: 02-Dec-2016].
- [49] E. Rojas-Nastrucci *et al.*, "Characterization and Modeling of K-Band Coplanar Waveguide Digitally Manufactured using Pulsed Picosecond Laser Machining of Thick-Film Conductive Paste."
- [50] M. F. Cordoba-Erazo, E. A. Rojas-Nastrucci, and T. Weller, "Simultaneous RF electrical conductivity and topography mapping of smooth and rough conductive traces using microwave microscopy to identify localized variations," in *Wireless and Microwave Technology Conference (WAMICON), 2015 IEEE 16th Annual*, 2015, pp. 1–4.
- [51] M. F. Córdoba-Erazo and T. M. Weller, "Noncontact Electrical Characterization of Printed Resistors Using Microwave Microscopy," *IEEE Trans. Instrum. Meas.*, vol. 64, no. 2, pp. 509–515, Feb. 2015.

Vita

Harvey Tsang earned his Bachelor of Science in Electrical Engineering degree from the University of Texas at Arlington in 2009. In 2011, he received his Master of Science in Electrical engineering degree from the University of Texas at El Paso, where he met his advisor, Dr. Kenneth Church. In 2011, he joined the doctoral program in Electrical Engineering at the University of Texas at El Paso.

While pursuing his Masters degree, he worked as a research assistant at nScript and continued with his research at Sciperio. At Sciperio, he worked on numerous R&D projects funded by federal, state and various private institutions and co-published a few IEEE papers with UTEP's EM Lab involving 3D printed antennae, all dielectric RF devices, and electromagnetic devices with metamaterials. During his doctoral degree, he collaborated with Dr. Thomas Weller and the students in the WAMI at the University of South Florida, where he co-published a few IEEE papers on 3D printed antennas and new 3D printing techniques. During his last year, he accepted a position at the Army Research Labs at Adelphi where he continues his research in 3D printed RF devices. At the time of this publication he works with Army Research Labs at Adelphi.

Permanent address: 1203 Fidler Ln, APT: 502
Silver Spring, MD, 20910

This dissertation was typed by Harvey Tsang.